

University of Alberta

Real Time Tracking of Lung Tumours Using Low Field MRI:

A Feasibility Study

by

Eugene Yip

A thesis submitted to the Faculty of Graduate Studies and Research

in partial fulfillment of the requirements for the degree of

Master of Science

in

Medical Physics

Department of Oncology

©Eugene Yip

Spring 2012

Edmonton, Alberta

Permission is hereby granted to the University of Alberta Libraries to reproduce single copies of this thesis and to lend or sell such copies for private, scholarly or scientific research purposes only. Where the thesis is converted to, or otherwise made available in digital form, the University of Alberta will advise potential users of the thesis of these terms.

The author reserves all other publication and other rights in association with the copyright in the thesis and, except as herein before provided, neither the thesis nor any substantial portion thereof may be printed or otherwise reproduced in any material form whatsoever without the author's prior written permission.

Abstract

The aim of this work is to evaluate the feasibility of low field MR based real time lung tumour tracking, a promising application of proposed linac-MR system. In this work, motion phantoms replicating low field MR contrast parameters for thoracic anatomy of lung cancer patients are imaged with fast imaging sequences in 3 T MRI. Noise is added to generate "low field equivalent" images. Using these phantom images, the accuracy of auto-segmentation was demonstrated by comparing the determined tumour shapes against reference shapes, and by comparing the determined tumour location against the independently measured reference tumour motion trajectory. Low field equivalent images are also generated for a lung cancer patient, and the tumour's shape and location determined via auto-segmentation. Low field MRI shows promise in terms of determining the shape and location of tumour in real-time such that it is feasible to track the moving tumours in real-time.

Acknowledgement

First and foremost, I would like to thank my mother, who has provided me with love and support for so many years.

Next, I would like to acknowledge my supervisor, *Cav. Fallone*, for his vision for linac-MR project, which will undoubtedly lead to a device that will make a significant impact to improve lives of cancer patients, while providing an excellent research opportunity for me. Next, I would like to extend my gratitude towards my co-supervisors, Dr. Satyapal Rathee and Dr. Keith Wachowicz for providing me with invaluable guidance and advice. I would also like to acknowledge the other members of my committee: Dr. Nick De Zanche, Dr. Atiyah Yayha and Dr. Richard Thompson for contributions of their knowledge and expertise.

Furthermore, I would also like to acknowledge my collaborator Jay Yun, whose contribution is invaluable to this work. I would also like to thank the team of excellent machinists at the CCI machine shop, without whom many aspects of this project will not have been possible. Not to be forgotten are my many other colleagues in the medical physics department, for providing me with (mostly good) advice, insights and much laughter.

Finally, I would like to thank the National Science and Engineering Research Council, and the Alberta Innovates-Health Solutions, for their financial support.

Table of Contents

Chapter 1 Introduction.....	1
1.1 - Background.....	1
1.2 - Radiation Target Volumes - Basic Definitions.....	3
1.3 - Image Guidance in Radiation Therapy.....	5
1.3.1 - Image Guidance Based on Fiducial Markers.....	5
1.3.2 - Image Guidance by Direct Imaging of Soft Tissues.....	6
1.3.3 - Linac-MR Hybrid Systems.....	8
1.4 - Respiratory Motion in Radiation Therapy.....	9
1.4.1 - Encompassing the Entire Volume of Motion.....	9
1.4.2 - Breath-hold Methods.....	11
1.4.3 - Gating Methods.....	11
1.4.4 - Tumour Tracking Methods.....	13
1.5 - Determining Tumour Position in Real Time.....	14
1.6 - Real Time MR Imaging of the Lung.....	14
1.7 - Objectives.....	17
1.8 - Thesis Organization.....	19
1.9 - References.....	19
Chapter 2 Theory.....	22

2.1 - Magnetic Resonance Physics	22
2.1.1 - Spins in a Magnetic Field.....	22
2.1.2 - Statistical Mechanics and Net Magnetization	23
2.1.3 - Magnetic Precession.....	25
2.1.4 - Bloch's equation and MR Relaxation.....	26
2.1.5 - Rotating Frame of Reference	28
2.1.6 - RF (B_1) Tipping Pulse	28
2.1.7 - T_2 and T_2^*	29
2.1.8 - MR Signal Detection.....	30
2.2 - Imaging Principles	31
2.2.1 - Fourier Transform	31
2.2.2 - Magnetic Field Gradients.....	32
2.2.3 - Slice Selection.....	33
2.2.4 - Frequency Encoding and Quadrature Detection	34
2.2.5 - Phase Encoding	36
2.3 - Spin Echo based Imaging Sequences.....	38
2.3.1 - Spin Echo Sequence.....	38
2.3.2 - Multiple Spin Echo Sequence as a T_2 Measurement Tool.....	40
2.3.3 - Inverse Recovery Sequence as a T_1 Measurement tool.....	41
2.3.4 - Turbo Spin Echo Sequences.....	43

2.4 - Gradient Echo Imaging	44
2.4.1 - FLASH Sequence	44
2.4.2 - SSFP-FID and SSFP-Echo	45
2.4.3 - Balanced SSFP	46
2.5 - Signal, Noise, and Contrast.....	48
2.5.1 - Signal-to-Noise Ratio.....	48
2.5.2 - Contrast to Noise Ratio	50
2.6 - Effects of Changing Main Magnetic Field Strength	51
2.6.1 - SNR Dependence on B_0	51
2.6.2 - Relaxation Values Dependence on B_0	52
2.6.3 - Specific Absorption Ratio	55
2.6.4 - CNR.....	55
2.7 - References.....	56

Chapter 3 A MR Lung Contrast Phantom.....57

3.1 - Overview.....	57
3.1.1 - Relative Proton Density	57
3.1.2 - T_1 Relaxation Times for Lung Tumour and Tissue.....	58
3.1.3 - T_2 and T_2^* Relaxation Times for Lung Tumour and Tissue	59
3.2 - Materials and Methods.....	60
3.2.1 - Phantom Materials for Simulated Tissues.....	60

3.2.2 Verification of Contrast Parameters	62
3.2.3 - Sequence Evaluation	64
3.3 - Results.....	65
3.3.1 - Parameter Maps.....	65
3.3.2 - Sequence Evaluation	68
3.4 Discussion	69
3.4 - References.....	70
Chapter 4 - Real Time Tumour Tracking Study	71
4.1 - Overview.....	71
4.2 - Materials and Methods.....	71
4.2.1 - Phantom Experiment Setup.....	71
4.2.2 - Tumour Shapes and Motion Patterns	73
4.2.3 - MR Imaging Sequences	75
4.2.4 - Image Post Processing.....	77
4.2.5 - CNR Measurements	78
4.2.6 - Data Analysis	79
4.2.7 - Contour Shape Fidelity.....	79
4.2.8 - Centroid Position Accuracy	80
4.3 - Results.....	81
4.3.1 - Simulated Lung Tumour Images with Low Field CNR.....	81

3.3.2 - CNR of Acquired Images	82
4.3.3 - Contour Shape Fidelity.....	83
4.3.4 - Centroid Position Accuracy	84
4.4 - Discussion.....	85
4.5 - References.....	88

Chapter 5 Initial Experience in-vivo Patient Tumour89

5.1 - Overview.....	89
5.2 - Methods and Materials.....	89
5.2.1 - Dynamic MR Imaging Sequence	90
5.2.2 - CNR Measurement and Comparison to Phantom Results	91
5.2.3 - CNR Modification of Images for Tumour Tracking	91
5.2.4 - Tumour Tracking of <i>in-vivo</i> 0.2 T/0.5 T Equivalent Images	91
5.2.5 - Tumour Tracking Data Analysis.....	92
5.3 - Results and Discussion	92
5.3.1 - CNR Measurements	92
5.3.2 - Tumour Tracking with 3 T CNR (Gold Standard).....	93
5.3.3 - Tumour Tracking with 0.2/0.5 T	94
5.4 - Discussion.....	95
5.4 - References.....	97

Chapter 6 - Conclusions.....98

6.1 References 101

Bibliography.....102

List of Tables

Table 3.1 MR contrast parameters of the 0.2 T equivalent lung phantom compared against literature values. Measured contrast parameters are expressed as mean \pm SD of pixel values within a region of interest.....	68
Table 3.2 MR contrast parameters of the 0.5 T equivalent lung phantom compared against literature values. Measured contrast parameters are expressed as mean \pm SD of pixel values within a region of interest.....	68
Table 4.1: CNR for spherical and non-spherical tumour models in 0.5 T and 0.2 T equivalent images. The standard deviation of the CNR is given in brackets.	83
Table 4.2: Dice's Coefficient, centroid error and RMSE in auto-contouring and tracking	84

List of Figures

Figure 1-1: Schematic Diagram representing the 3 target volumes. GTV represents the visible tumour in the image. CTV includes the GTV and a margin to account for microscopic disease. PTV includes an additional margin to the CTV, accounting for mechanical uncertainties and organ motion.	5
Figure 1-2: Linac-MR with perpendicular field designs, the magnetic field strength in this design is limited in this configuration as the interaction between electrons and the magnetic field cause unfavorable dose distribution in the patient. Figure courtesy of Emanuel Blosser.	16
Figure 1-3: Linac-MR with parallel field design, magnetic field can be increased this design because the magnetic field does not create undesirable dose distribution within the patient. Figure courtesy of Emanuel Blosser.....	17
Figure 2-1: Sequence diagram for a spin echo sequence. RF describes the radiofrequency pulse, G_x, G_y, G_z describes the x, y, z gradients, and Acq. describes the acquired signal. TE is the echo time, and TR is the repetition time.	40
Figure 2-2: Sequence diagram for a multi-spin echo sequence.	41
Figure 2-3: Sequence diagram for an inverse recovery sequence.....	43
Figure 2-4: Sequence diagram of the FLASH sequence. Random gradients are employed to spoil the remaining transverse magnetization at the end of each TR interval.	45
Figure 2-5: Sequence diagram for the SSFP-FID sequence (Top) and the SSFP-echo sequence (Bottom). They are mirror image of each other.....	46
Figure 2-6: Sequence diagram for the balanced SSFP sequence.....	48

Figure 2-7: Sample spectral density for protons in 3 different environments. Blue curve represents protons in a tightly bound environment, green curve represents protons in free water, and the red curve represents water in most tissues, which is an intermediate between the other two extreme cases	53
Figure 3-1: T_1 dependence on magnetic field strength for normal lung tissue and lung tumours.	58
Figure 3-2: T_1 relaxation curve for a representative tumour pixel from the 0.2 T phantom. The data point at 300 ms (the point closest to the null point) is discarded, and the data point at 100 ms and 200 ms are inverted. Signal is expressed in relative units.	63
Figure 3-3: 32 echo T_2 relaxation curves for the tumour and normal tissue for the 0.2 T phantom. Signal is expressed in relative units.....	64
Figure 3-4: T_1 (in ms) parameter map of the lung compartment of the 0.2 T (left) and the 0.5 T (right) equivalent phantom.....	66
Figure 3-5: T_2 (in ms) parameter map of the lung compartment of the 0.2 T (left) and the 0.5 T (right) equivalent phantoms.	67
Figure 3-6: PD maps for lung compartment of the 0.2 T (left) and 0.5 T (right) equivalent phantoms.	67
Figure 4-1 Schematic diagram of the experiment set up	73
Figure 4-2: Motion Patterns used to drive lung compartment. A sine pattern (upper left) and three lung tumour motion patterns from patient data.....	75
Figure 4-3 First row, from left to right: 1) High Resolution TSE (middle slice) image. 2) Noise added (0.5 T) dynamic bSSFP scan. 3) High Resolution TSE	

(middle slice) image for a non spherical tumour. 4) Corresponding noise added (0.5 T) dynamic bSSFP scan. Second row: equivalent images for 0.2 T experiments..... 82

Figure 4-4: Sample dynamic bSSFP images from the experiment, after noise addition. Image on the left reflects 0.5 T equivalent CNR whereas image on the right reflects 0.2 T equivalent CNR..... 83

Figure 5-1: A transverse view of the patient. The solid tumour is indicated by the red arrow. The blue dotted lines encompass the thick sagittal imaging plane used in cine imaging..... 90

Figure 5-2: Sample dynamic images of the patient for the original 3 T image (left), noise added to reflect 0.5 T CNR (centre) and 0.2 T CNR (right). Lung tumour in each image is indicated by a red arrow. 93

Figure 5-3: Centroid position of auto-segmented tumour (AP) in 3 T images as determined by the auto-contouring algorithm. The maximum range of AP motion is 5.7 mm..... 94

Figure 5-4: Centroid position of auto-segmented tumour (SI) in 3 T images as determined by the auto-contouring algorithm. The maximum extent of SI motion is 26.1 mm..... 94

Chapter 1 Introduction

1.1 - Background

As of 2008, Cancer remains the leading cause of death in developed countries and the second leading cause of death in developing countries - responsible for a annual global death toll of 7.6 million [1]. Of the world's population, approximately one third of them will develop cancer at some point in their lives, and approximately one-fourth will die from it [2]. In addition to loss of life, cancer is a major drain to the economy, costing more than \$17.1 billion in Canada alone [3], both in terms of direct healthcare cost and loss in productivity.

An intensive scientific effort has been underway to develop and improve methods to prevent, diagnose and treat cancer. Medical physicists have made significant contributions to these developments, which have led to new technologies that have significantly improved in survival rates and quality of life for cancer patients. Two areas in which physicists have played a major role are radiation therapy and medical imaging.

Radiation therapy is the clinical application of ionizing radiation for treatment of diseases, and can be used with either curative or palliative intent. Currently, about half of all cancer patients will receive some form of radiation treatment.

The goal of the radiation therapy process is to deliver a high dose of radiation to a specific target volume while minimizing the dose to surrounding healthy tissues.

Radiation can be delivered internally by using radioactive implants, as in the case of brachytherapy, or it can be delivered using an external beam. Over the course

of the 20th century, a variety of technologies have been developed to deliver radiation treatment. Coolidge tube was developed early in the century, with tubes capable of generating a peak energy of 140 kilovolts (kV) in 1913 and 200 kV in 1920[2]. Therapeutic beams of megavoltage (MV) energy were achieved in the 1940's with the betatron unit[4]. The Cobalt-60 system was developed in Canada and was used to treat cancer patients for the first time in 1951[2]. In 1953, the first medical linear accelerators (linacs) were built in England and reached clinical status in the 1960's [2]. Today, the vast majority of radiation therapy treatments in the developed world are delivered using Linac technologies.

Medical Imaging is the clinical application of various techniques to create images that allows one to visualize human anatomy and physiology. Imaging has broad range of applications in cancer; it is an important early detection and diagnostic tool for many types of cancers, and it is also an integral part of the radiation therapy planning and verification processes. Two-dimensional (2D) imaging modalities such as radiography, mammography and fluoroscopy, are still commonly used in clinics today. More advanced modalities which are capable of three-dimensional (3D) imaging include computed tomography (CT) , single photon emission computed tomography (SPECT), positive emission tomography, (PET), ultrasound and magnetic resonance imaging (MRI).

The developments of more advanced 3D imaging modalities in the 1970's (CT and MRI) have led to a major improvement in the radiation therapy (RT) process, known as 3D conformal radiation therapy (3D-CRT) [2]. In the 3D-CRT process, the physician defines a specific 3D target volume in the images. The radiation

treatment planning system (RTPS) employs a number of different treatment beam orientations to accurately cover a complex target shape. More recently, Intensity Modulated Radiation Therapy (IMRT) is introduced which uses an inverse iterative algorithm for plan optimization, and dynamic multi-leaf collimator (dMLC) for beam delivery [2]. IMRT allows for further escalation dose to the target while maintaining tolerable doses to surrounding tissue. IMRT represent the state of the art technology available today for in terms of radiation dose delivery.

1.2 - Radiation Target Volumes - Basic Definitions

IMRT based treatment plans can have very sharp dose fall off away from the intended treatment volume. Therefore positional accuracy of the treatment volume with respect to the beam geometry, is of paramount importance. Several important concepts and standard terminology for this topic, as defined by the International Commission of Radiation Units and Measurements (ICRU) report no. 50 [5], are introduced in this section. These definitions, among other issues, specifically address the uncertainty in positioning the patient and the treatment volume .

On an image, the **Gross Tumour Volume (GTV)** is the visible extent and location of the malignant growth, and GTV may include the primary tumour site, metastatic lymph nodes and other metastases. However, due to limitations of imaging modalities, microscopic malignant cells cannot be adequately visualized, therefore, a **clinical target volume (CTV)** is defined by the physician to include both the GTV and the extent of microscopic diseases that surrounds it. The ideal

goal of radiation therapy is to deliver a uniform, therapeutic dose of radiation to this volume spanned over a large number (typically 30) of daily fractions.

Several factors introduce uncertainty in the radiation therapy process. They include 1) the daily set-up of patient, and 2) mechanical components of radiation therapy machine and 3) organ motions. These uncertainties make it difficult to align the CTV to the treatment beam in each fraction. To account for these uncertainties, a **planning target volume (PTV)** is defined to include the CTV and a margin to account for these errors, to ensure that the CTV will receive the prescribed radiation dose. Of the three factors that contribute to the geometric uncertainty, the mechanical tolerance of the radiation therapy treatment machine is the least contributing factor. Patient setup can be improved by employing some form of imaging which is, at least, capable of imaging bony anatomy of the patient in the treatment position. The most significant, and also the most difficult to circumvent, factor is the organ motion. It is important to distinguish between two types of organ motions: *inter*-fractional organ motion, which is the organ motion that occurs in the timescale of the days of treatment (such as a shrinking of the tumour as a response to treatment) an *intra*-fractional organ motion, which is the type of motion the occurs during treatment, such as organ motion that is associated with respiration. A PTV margins must account for all of these errors. A schematic diagram showing the 3 types of target volumes are shown in Figure 1-1.

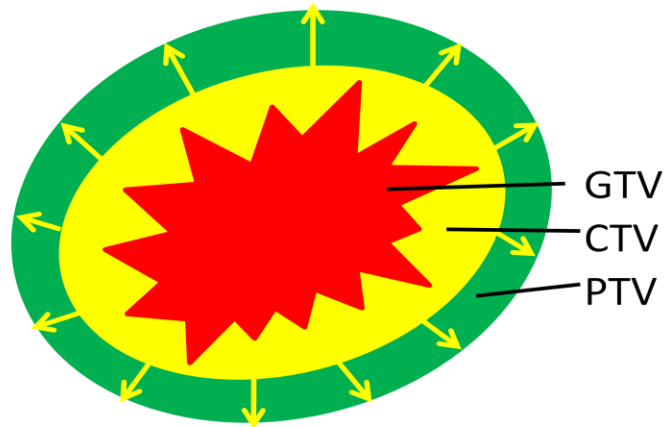


Figure 1-1: Schematic Diagram representing the 3 target volumes. GTV represents the visible tumour in the image. CTV includes the GTV and a margin to account for microscopic disease. PTV includes an additional margin to the CTV, accounting for mechanical uncertainties and organ motion.

1.3 - Image Guidance in Radiation Therapy

The main advantage of modern radiotherapy, i.e. via IMRT, of delivering a high dose to the CTV while sparing normal tissues cannot be fully realized if there is a large PTV margin. Therefore, considerable research has been done to develop methods to reduce these margins. One major effort has been the incorporation of imaging devices with radiation therapy treatment units. The form of RT in which images are used daily to align the patient (of the CTV if visible), with the treatment beam for the purpose of reducing PTV margin is known as the image guided radiation therapy (IGRT).

1.3.1 - Image Guidance Based on Fiducial Markers

A relatively simple addition to the linac that allows 2D projection imaging, akin to the conventional radiography, is a portal imaging device. In this approach, a film or a digital detector such as electronic portal imaging devices (EPID) is used to acquire an image using the x-ray photons of the treatment beam [6]. The

significant drawback of portal imaging using MV photons is the extremely poor soft tissue contrast that limits the use of portal imaging to visualizing bony structures alone. Most tumours are far away from bony markers and their independent motion relative to bones makes it an ineffective approach to reduce PTV margins [7]. Implanted fiducial markers are therefore inserted near or inside the tumour. Measured locations of the fiducials in the portal images then serve as the surrogate of tumour position in the patient, which can be used for daily alignment of the tumour with the treatment. If the fiducial based guidance is successful then it can potentially reduce the PTV margins; however, there are several issues with this approach including: 1) fiducial insertion is an invasive procedure and can result in infection [9]; 2) not all treatment sites are amenable to fiducial insertion; 3) fiducials can migrate from their initial location during the treatment[10]; resulting in a poor correlation between fiducial and tumour position, and finally 4) the fiducials images do not provide any information regarding the tumour's shape and volume changes. Further improvement to this approach is provided by the introduction of peripheral kV energy x-ray units into the treatment room [8]. While soft tissue contrast remains limited in kV projection images, bony contrast and the contrast of radio-opaque fiducial markers are significantly improved, while the additional radiation dose to the patient resulting from imaging is reduced.

1.3.2 - Image Guidance by Direct Imaging of Soft Tissues

To overcome some of the shortcoming of fiducial marker based IGRT techniques, other devices have been developed to directly image the tumour and the

surrounding tissues. Ultrasound imaging devices have been proposed as an in-room imaging modality for soft tissue visualization. However, the utility of ultrasound imaging is limited to the visualization of soft-tissue, albeit poorly, in pelvic and abdominal regions [8]. The imaging quality is strongly correlated with the operators' skill and experience level. In addition, the operator is required to operate the probe during the imaging process which makes it difficult to use this system while the radiation beam is on. Thus, the system is limited to pre-treatment image guidance and not suitable for real-time IGRT.

Diagnostic CT devices have also been introduced into the treatment room which allows for limited soft tissue imaging [8]. In these systems, the patient will be transferred in and out of the CT gantry using a couch, or the treatment unit itself may be moved into position using rails [11]. Unfortunately, uncertainties may arise during the transition from CT imaging and beam delivery. Moreover, many soft-tissue solid tumours are poorly visualized in CT imaging. Another alternative approach is to acquire cone-beam volumetric CT (CBCT) images by integrating a kV source and an active matrix flat panel imaging detector onto the linac gantry [12], orthogonal to the treatment beam direction. The disadvantage of a gantry-mounted cone-beam imaging system is scattered radiation that degrades the quality of CT images obtained from these systems [8]. Additional weight on the gantry may cause it to sag, reducing the mechanical accuracy of the overall treatment system [8]. Full integration of the treatment unit and imaging device is achieved with the Tomotherapy device [13]. In this system, a 6 MV linac is mounted on a ring-shaped gantry and it rotates continuously while the patient

translates through the axis of rotation of the gantry. From the perspective of the patient, the treatment beam is delivered in a helical manner. Conceptually, the tomotherapy unit can be thought of as a CT unit in which the kV source is replaced with a 6MV Linac. The tomotherapy unit can operate in CT imaging mode to provide pre-treatment cross-sectional images of the bony anatomy of the patient; however soft-tissue contrast in these images is significantly poorer than the diagnostic CT images.

Many of these IGRT methods are beneficial in reducing the patient set up errors in terms of aligning bones. In that sense, the inter-fractional displacement of bony anatomy is reduced which provides some reduction of PTV margins. However, they have a limited capability of directly aligning the tumour with the treatment beam and are definitely not able to directly image the moving tumours in real-time while the treatment beam is delivering radiation.

1.3.3 - Linac-MR Hybrid Systems

One exciting development in IGRT technology is the integration of a Linac unit with a magnetic resonance imaging device [14,15]. In principle, this approach offers numerous advantages. MR offers vastly superior soft tissue contrast compared to the methods mentioned previously. Improved visualization of tumour and surrounding soft tissues may further reduce set up uncertainties. Another benefit of the MR imaging is that because MR imaging relies on non ionizing RF pulses, no additional dose will be delivered for patient set up, which can be significant [16]. Another potential benefit of the Linac-MR system is large flexibility in MR imaging sequences, including some sequences that are capable

of generating several images per second. Therefore, the system can, in principle, provide real time, intra-fractional tracking of moving tumours using volumetric images of the tumours and surrounding tissues. This application is not possible with the other systems mentioned in the previous section. The Linac-MR unit could represent a major breakthrough in IGRT technology.

1.4 - Respiratory Motion in Radiation Therapy

The organ motion caused by the patient's respiratory process creates a considerable challenge in radiation therapy. Various studies in lung tumour motion have observed a complex 3D trajectory, with the superior-inferior (SI) direction being the predominant motion. Reports of range of tumour motion vary widely, with the maximum motion reported being 50 mm in the SI direction, 24 mm in the anterior posterior (AP) direction and 16 mm in the left right (LR) direction [17]. Respiration motion also is reported in abdominal organs such as pancreas, liver, kidney and the diaphragm. This section covers some of the common strategies in addressing respiration motion in radiation therapy.

1.4.1 - Encompassing the Entire Volume of Motion

In order to deliver the prescribed radiation dose to the CTV, the PTV margins must be expanded such that it accounts for organ motion. Imaging techniques have been used to create images that would encompass the entire volume of motion. Free-breathing, slow CT scans are used to image the moving tumour so that the image is acquired over several phase of respiration [18]. This causes the tumour signal on the image to be blurred out over the entire volume of motion. The motional blurring also reduces the resolution of the image, which may lead to

increasing inter and intra-observer variability in GTV/CTV contours [17].

Another approach is to acquire CT images while the patients are holding their breath. Two sets of images are acquired: one at inhalation and the other at exhalation. After the appropriate image fusion and registration, a maximum intensity projection (MIP) from the two image sets is generated, creating the motion encompassing volume [19]. Breath-hold technique creates less blurred images than the slow CT method, but requires twice the scan time and radiation dose [17]. The drawback of this approach is that it is limited by the ability of the patient to hold their breath, which is compromised in many lung cancer patients.

4D-CT is a promising new method for CT imaging of lung tumours [17]. In a typical 4D-CT scan, due to the inherent imaging speed limitation by the rotation of the gantry, the different slices in a single 3D acquisition will be in a different phases of the breathing cycle. Therefore, in a typical in 4D-scan, about 8-25 complete CT data sets are reconstructed, and the 3D volumes are "sorted" in the correct phases during post processing [17]. Using these 3D volumes at different phase of the cycle, the 3D trajectory of the moving tumour can be reconstructed. The drawbacks of 4D-CT are that its accuracy is affected by any variations in the patient's breathing pattern [17], and it subjects patient to additional radiation dose. As 4D CT images are reconstructed after data is acquired for several breathing cycles, it is not a true real time imaging modality.

Encompassing the entire range of tumour motion in the PTV will ensure that the CTV receives the prescribed dose. However, the major disadvantage of this method is the large resulting CTV to PTV margin includes a significant amount of

normal tissue in the prescribed dose volume which may lead to increased normal tissue complications.

1.4.2 - Breath-hold Methods

Another way of managing respiratory motion is to ask the patients to hold their breath during treatment planning CT imaging and while the radiation is being delivered. In addition to significantly reducing the intra-fraction motion due to breathing, if a patient can maintain a deep inspiration breath hold (DIBH) position [20], their thoracic anatomy is often positioned in such a way that the critical organs are located further away from the PTV due to the increase in the volume of the lung. Therefore, the critical organs are better protected as a result.. A spirometer monitors the level of inspiration in the patient to improve reproducibility. For treatment planning, three CT scans are required, a free breathing CT scan, a spirometer monitored DIBH CT scan, and a spirometer inhalation scan.

Treatment planning is performed on the DIBH CT scan while the free breathing and the inhalation image sets are used for quality assurance, and to generate an alternative treatment plan if the DIBH is unsuccessful. In general, the applicability of breath-hold technique is limited by patient compliance. In the DIBH study, 60% of lung cancer patients were not able to maintain their breath with the required degree of reproducibility for the DIBH treatment [17].

1.4.3 - Gating Methods

Respiratory gating is another approach to address breathing motion. The concept of "gating" is to only deliver radiation when the tumour is located in a specified window in the respiratory cycle. There are numerous gating techniques available

[17], and they are performed using an external motion detectors or internal fiducial markers. A gated set of CT images are typically required during the CT simulation session for gated therapy. Fiducial markers or the external tumour motion surrogates are used to generate a "respiratory signal" that is assumed to correlate with respiratory phases of lung motion. When the respiratory signal is within the preset gating window, the CT scanner acquires a single CT slice. The time required to acquire this single slice should be matched with the "gate width". A gate width that is too large the image will not fully encapsulate the motion within the gating window, resulting in a tumour that appears too small to account for the motion within the gating window. If the gate width that is too small compared to the scan-time, the opposite is true; the image captures motion that does not belong in the gating window, resulting in a tumour that appears too large. The gating process is time consuming because only a single slice of the 3D volume is acquired per breathing cycle. For beam delivery, a similar procedure is performed, with the radiation beam being delivered when the respiration signal falls within the gating window. As these methods use fiducial markers, more typically the external motion monitoring devices, as a surrogate for the tumour motion, it suffers from all the limitations as mentioned in section 1.3.1 [17]. Comparing to motion encompassing methods, gating technique can significantly reduce PTV margins and dose to normal tissues. This improvement does come with a cost, as the beam is only on for a narrow portion of the breathing cycle, treatment time will be significantly increased [17].

1.4.4 - Tumour Tracking Methods

Another approach is to image the moving tumour during irradiation and move the radiation beam so that tumour and radiation beam are always aligned. This procedure is commonly called tumour tracking. In principle, this approach eliminates the main disadvantages from the other techniques [17]. Compared to the tumour encompassing methods, the ability for the beam to follow the tumour trajectory can substantially reduce PTV margins. Patient compliancy will be significantly less challenging as breath-hold is not required. Since radiation is continuously delivered while repositioned in real time, tumour tracking methods will not increase the treatment time to the degree of the gated methods.

There are several aspects of real time tumour tracking. Firstly, the position of the tumour must be determined in real time. Secondly, all tumour tracking devices will have a significant delay time between imaging and radiation delivery (imaging time, computer processing time, multi-leaf collimator motion (MLC) delay etc.). This must be in some ways compensated by a prediction algorithm. The accuracy of these prediction algorithm decay rapidly with increased delay time, therefore a delay time of more than 0.5 seconds is not considered suitable for tumour tracking [17]. Thirdly, the beam must be repositioned in real time, either by motion of the Linac head, or by movement of the MLC. Lastly, any dosimetric effects of breathing (such as the change in air volume) that is not captured by the static treatment planning images may lead to second-order dosimetry errors. The degree of impact of these effects require further investigation[17.]

1.5 - Determining Tumour Position in Real Time

Several methods are under development for determining the position of tumours in real time. An external surrogate can be used in principle to predict the location of the tumour, however, the complex and non-stationary correlation between these surrogates and the actual tumour could lead to uncertainties. Direct imaging of the tumour will eliminate these uncertainties but acquiring an image with the constraint of a delay time under 0.5 seconds is a considerable challenge. Of the IGRT devices available, fluroscopy devices (such as the Cyberknife system[21]) are capable of generating images in real time, but these images do not have sufficient soft tissue contrast for visualization and auto-segmentation of tumours, and fiducial markers are therefore needed which come with all of the associated disadvantages mentioned previously. The proposed Linac-MR device, in principle, does have real time soft tissue imaging capabilities. However, MR imaging is inherently based on a tradeoff between image quality and image acquisition speed. Whether or not the images generated in these conditions have sufficient quality for auto-contouring of tumours will need to be assessed.

1.6 - Real Time MR Imaging of the Lung

Lung MRI has traditionally been limited to diagnostic uses where image quality, rather than the “real time” acquisition speed, is of primary importance. However, recently, significant improvements in MRI hardware, the development of high speed dynamic imaging sequences, as well as methods to speed up data acquisition have made real time imaging of lung tumours feasible. The feasibility of real time tumour tracking has recently been demonstrated for a 1.5 T scanner

[22]. The feasibility of performing real time MR tumour tracking has yet to be demonstrated in a low field scanner. This is likely due to the fact that most diagnostic MRI scanners available in research centers (including this Cross Cancer Institute) use higher magnetic field strengths (> 1.5 T scanners). Higher field scanners generally provide a greater amount of signal to noise ratio for imaging, which is important for diagnostic use. However, for the purpose of real time IGRT, the strength of the MR magnetic field, in the integrated linac-MR systems, must be chosen with careful consideration of both image quality and the impact of magnetic field strength and orientation on delivered radiation dose distributions within the patient. Physical interaction, known as the Lorentz force, between the magnetic field and the energetic, secondary electrons can have undesirable radiation hot and cold spots of radiation dose within the patient. The secondary electrons are generated by the interaction between the therapeutic photon beam and the tissue within the patient [23]. If the main magnetic field of the MR imager is oriented perpendicular to the direction of the treatment photon beam, a 1.5 T magnetic field causes significant amounts of overdosed and underdosed regions around the PTV as compared to a 0.2 T field. This is a highly undesirable outcome and may limit the field strengths of the Linac-MR to low fields. However, a different linac-MR design, in which the radiation beam is oriented parallel to the magnetic field of the MRI, the Lorentz force effect may actually be *beneficial* to the in-patient dosimetry [23]. This parallel design allows MR field strength higher than 0.2 T to be feasible, with the current proposed design using a 0.5 T magnet. In the parallel field design, considerations of skin

dose due to electrons generated in the beam upstream of the patient must be carefully made[24].

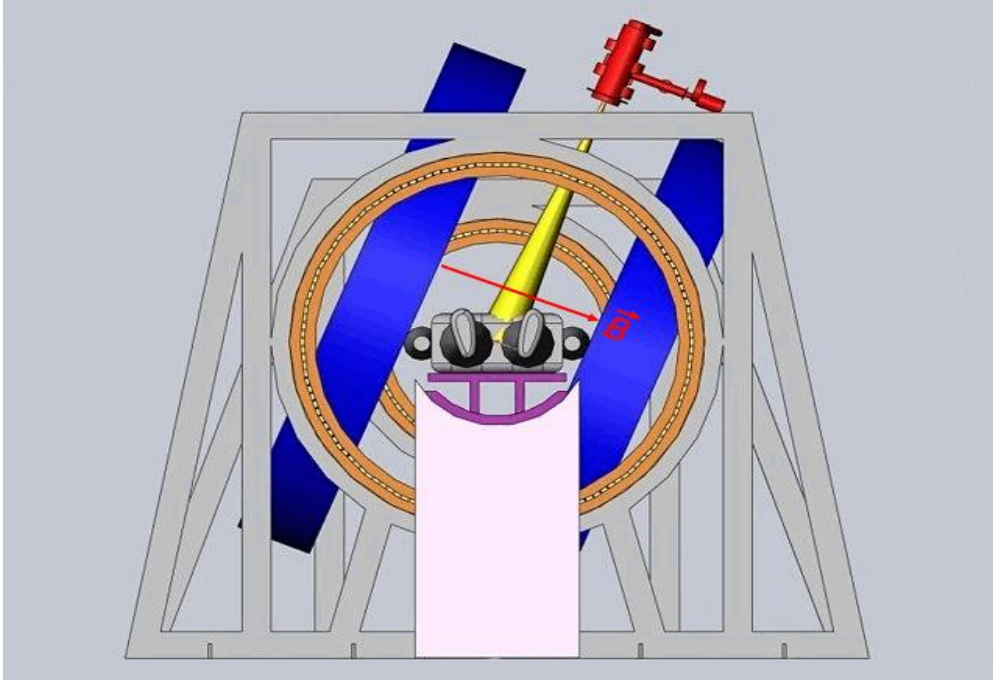


Figure 1-2: Linac-MR with perpendicular field designs, the magnetic field strength in this design is limited in this configuration as the interaction between electrons and the magnetic field cause unfavorable dose distribution in the patient. Figure courtesy of Emanuel Blosser.

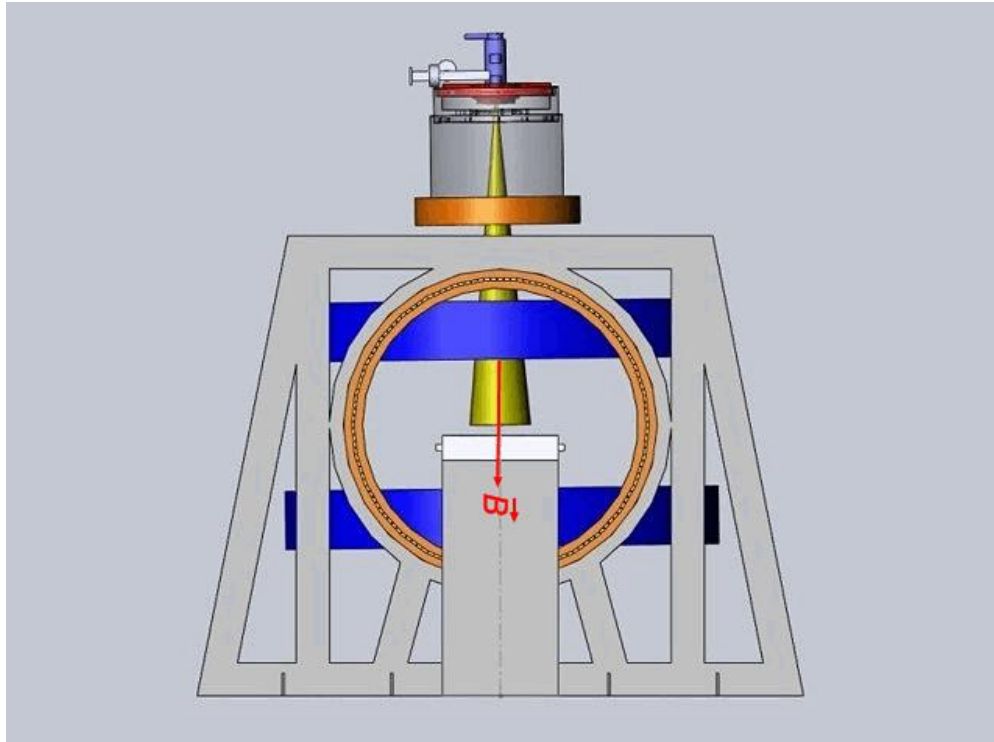


Figure 1-3: Linac-MR with parallel field design, magnetic field can be increased this design because the magnetic field does not create undesirable dose distribution within the patient. Figure courtesy of Emanuel Blosser.

1.7 - Objectives

Since there is a range of possible magnetic field strengths that could be used for a hybrid linac-MR design, the ability for MRI to create images for real time tumour tracking at these field strengths needs to be assessed. Ideally, patients with lung tumours can be imaged, with informed consent and ethics approval, with MR imagers at various field strengths, but that is not practical for a feasibility study. However, the MR properties (such as relaxation times) of lung tumour and lung tissue at various magnetic field strengths have been investigated and reported in the literature. Lung “mimicking” phantoms using different materials can be made to replicate these MR properties. Using these phantoms, images with similar quality to those acquired in low field strengths (0.2/0.5 T) can be obtained by

manipulating images acquired from a single MR scanner. Different types of dynamic MRI sequences can be evaluated using these phantoms to determine a suitable sequence for real time imaging of patients. Once a suitable imaging sequence is determined, the moving phantom with the motion patterns similar to breathing induced thoracic motion patterns in patients can be imaged. The “tumour” can then be segmented from these dynamic images using a suitable auto-contouring algorithm in order to test the efficacy of the entire process for tumour tracking. This will also quantitatively evaluate the accuracy of the auto-contouring. Thus, the feasibility of tumour tracking in both lower field strength can be evaluated in a single 3 T scanner.

In summary, there are three main objectives of this work. Firstly, lung phantoms are constructed to replicates the MR properties of both lung tumours and healthy lung parenchyma. Secondly, various dynamic MRI sequences are evaluated, and a suitable sequence, with sufficient acquisition speed to capture breathing motion and adequate image contrast to visualize lung tumours against background tissue is determined. These two are the fundamental requirements for real time tracking of lung tumours by the radiation beam. Finally, using the determined suitable MRI sequence, the dynamic images are acquired of the lung phantom undergoing realistic motion(s) derived from the previously obtained motion patterns of lung cancer patients. A tumour auto-contouring algorithm is also tested to investigate its accuracy and efficiency in segmenting dynamic images.

All MR experiments described in this thesis (Chapters 3 to 5) are performed in the Philips 3 T Intera system (Philips Medical Systems, Amsterdam, Netherlands),

and data analysis is performed using MATLAB R2010a (Mathworks, Natick, MA, USA).

1.8 - Thesis Organization

This chapter provided the basic background behind image guidance for radiation therapy, as well as the motivation behind this work. In the next chapter, the theories and physical principles behind magnetic resonance imaging is introduced, along with the important metrics of assessing imaging quality, such as contrast, contrast to noise ratio (CNR) and signal to noise ratio (SNR) etc. In the third chapter, the experiments that were used to construct the lung phantom and evaluate its relaxation times are described in details. The feasibility of real-time tumour tracking (“tumour” imaging and auto-segmentation) is presented in the fourth chapter. The fifth chapter contains some preliminary in-vivo works on lung tumour patients. Chapters 3-5 also contain the results and discussion from the corresponding experiments. Finally, the conclusions of this thesis, and the future research directions inspired from the implication of the results are given in the sixth chapter.

1.9 - References

1. World Health Organization. *World Health Statistics 2008*, 2008.
2. Van Dyk, J. *The Modern Technology of Radiation Oncology*. (Madison: Medical Physics Publishing), 1999
3. Health Canada, *Economic Burden of Chronic Illnesses in Canada 1998*, 2002
4. Laughlin, JS. *Development of Technology of Radiation Therapy*. *Radiography*, 9(6):1245, 1989
5. International Commission of Radiation Units and Measurements (ICRU). ICRU Report 50 "Prescribing, Recording, Reporting Photon Beam Therapy." 1993.

6. Dawson, LA., Jaffray, LA. *Advances in Image Guided Radiation Therapy*. Journal of Clinical Oncology 25(8):938, 2007.
7. Langen KM., Jones DT. Organ Motion and Its Management. International Journal of Radiation Oncology, Biology and Physics, 50:265, 2001.
8. Verellen, D, De Ridder, M, Linthout et al., Innovations in image-guided radiotherapy, Nature 7:949, 2007.
9. Rodgers MS, Collinson R, Desai et al., Risk of dissemination with biopsy of colorectal liver metastases. Dis Colon Rectum 46:454, 2003
10. Haddad FS, Somsin AA. Seeding and perineal implantation of prostate cancer in the track of the biopsy needle: three case reports and a review of literature. Journal of Surgical Oncology, 35:184, 1987.
11. Cheng CW, Wong J, Grimm L., Commissioning and Clinical Implementation of a sliding gantry CT scanner installed in an existing treatment room and early clinical experience for precise tumour localization. American Journal of Clinical Oncology. 26(3):e23, 2003.
12. Jaffray, DA, Siewerdsen, JH, Wing JW, Martinez, AA. Flat-panel cone-beam computed tomography for image-guided radiation therapy. International Journal of Radiation Oncology Biology Physics. 53:1337, 2002.
13. Mackie, TR, Kapatoes, J, Rachala, K, et al., Image guidance for precise conformal radiotherapy. International Journal of Radiation Oncology Biology and Physics 56(1):89, 2003.
14. Fallone, BG, Murray B, Rathee S et al., First MR images obtained during megavoltage photon irradiation from a prototype integrated linac-MR system. Medical Physics, 36(6):2094, 2009.
15. Raaymakers BW, Lagendijk JJW, Overweg J et al., Integrating a 1.5T MRI scanner with a 6 MV accelerator: proof of concept. Phys Med Bio. 54:N229, 2009.
16. Walter C, Heggemann, JB, Wertz, H et al., Phantom and in vivo measurements of dose exposure by image-guided radiotherapy (IGRT): MV portal images vs. kV portal images vs. cone-beam CT. Radiotherapy and Oncology 85:418, 2007.
17. Keall, PJ, Mageras GS, Balter JM et al., The management of respiratory motion in radiation oncology report of AAPM Task Group 76. Medical Physics, 33(10):3874, 2006
18. Lagerwaard FJ, Van Sornsen de Koste, JR, Nijssen-Vosser, MR, et al., Multiple "slow" CT scans for incorporating lung tumour mobility in radiotherapy planning. International Journal of Radiation Oncology Biology Physics, 51(4):932, 2001
19. Underberg RW, Lagerwaard FJ, Slotman BJ et al., Use of maximum intensity projections (MIP) for target volume generation in 4DCT scans for lung cancer, International Journal of Radiation Oncology Biology Physics, 63(1):253, 2005.
20. Hanley J, Debois MM, Mah D et al., Deep inspiration breath-hold technique for lung tumours: The potential value of target

immobilization and reduced lung density in dose escalation.
International Journal of Radiation Oncology Biology Physics. 45(3),
603, 1999.

21. Murphy MJ, Adler JR, Modduluri M. et al. Image guided radiosurgery for the spine and pancreas, *Comput. Aided Surgery* 5(4):278, 2000.
22. Plathow C, Klopp M, Fink C et al., Quantitative analysis of lung and tumour mobility: comparison of two time-resolved MRI sequence. *The British Journal of Radiology* 78:836, 2005
23. Kirkby C, Murray B, Rathee S, Fallone BG. Lung Dosimetry in a linac-MRI radiotherapy unit with a longitudinal magnetic field. *Medical Physics*, 37(9):4722, 2010
24. Oborn, BM, Metcalfe PE, Rosenfeld AB, Butson MJ. Monte Carlo Characterization of skin doses in 6 MV transverse MRI-linac systems: Effect of field size, surface orientation strength, and exit bolus. *Med. Phys*, 37(10):5208, 2010

Chapter 2 Theory

2.1 - Magnetic Resonance Physics

2.1.1 - Spins in a Magnetic Field

The atomic nuclei are made of elementary particles (i.e. protons, neutrons) which contain a fundamental property known as magnetic spins. Atoms with nuclei containing an odd number of protons and/or an odd number of neutrons possess an intrinsic angular momentum, which gives rise to a magnetic dipole moment, m [1]

$$\mathbf{m} = \gamma \mathbf{S} \quad (2.1)$$

where γ is a constant known as the gyromagnetic ratio (2.68×10^8 rad/s/T for ^{1}H protons), and \mathbf{S} is the spin angular momentum. For atomic nuclei with a non-zero magnetic dipole moment, nuclear magnetic resonance (NMR) occurs in the presence of external magnetic fields. The magnetic moment interacts with the external magnetic field, which gives rise to the energy [1]

$$E = -\mathbf{m} \cdot \mathbf{B} \quad (2.2)$$

where vector \mathbf{B} is the external magnetic field. If the magnetic field is applied in the z direction, that is, $\mathbf{B} = B_0 \hat{\mathbf{z}}$, then the energy can be calculated as

$$E = -m_z B_0 = \gamma S_z B_0 = -\gamma \hbar s B_0 \quad (2.3)$$

From quantum mechanics it is known that S_z , the z -component of spin angular momentum, can exist only in certain quantized states, or $\hbar s$, where \hbar is Planck's

constant (1.05×10^{-34} J.s), and s is the spin quantum projection number. For a spin $\frac{1}{2}$ particle such as a proton, s can only take two possible values: $+1/2$ or $-1/2$. This gives rise to a high energy “spin down” state and a low energy “spin up” state, with an energy difference of

$$\Delta E = \gamma \hbar B_o \quad (2.4)$$

2.1.2 - Statistical Mechanics and Net Magnetization

For each of the energy states, E_+ and E_- , the fraction of particles occupying an energy state is described by the Boltzmann’s distribution, which states that [2]

$$\frac{N_+}{N} = \frac{e^{\frac{-E_+}{k_b T}}}{Z} \quad (2.5)$$

$$\frac{N_-}{N} = \frac{e^{\frac{-E_-}{k_b T}}}{Z} \quad (2.6)$$

and

$$Z = e^{\frac{-E_+}{k_b T}} + e^{\frac{-E_-}{k_b T}} \quad (2.7)$$

is the partition function for this two state system. N is the total number of particles and, N_+ and N_- are the number of particles with the energies E_+ and E_- , respectively. The constant k_b is the Boltzmann’s constant, and T is the temperature of the sample. Using these equations, one can calculate the ratio between these two states as follows [2]

$$R = \frac{N_-}{N_+} = e^{\frac{\Delta E}{k_b T}} \quad (2.8)$$

In the case where the magnetic field is at 3.0 T and a body temperature of $T = 310\text{K}$, $\frac{\Delta E}{k_b T} = 2.0 \times 10^{-5}$, R can be approximated, using the Taylor's series, as

$$R = e^{\frac{\Delta E}{k_b T}} \approx 1 + \frac{\Delta E}{k_b T} = 1.000020 \quad (2.9)$$

The excess amount of low energy “spin up” state will give rise to a net magnetization, given as

$$\begin{aligned} M_0 &= m(N_+ - N_-) = m(N_+ + N_-) \frac{(N_+ - N_-)}{(N_+ + N_-)} \\ &= mN \frac{R - 1}{R + 1} \end{aligned} \quad (2.10)$$

substitution in the equation, one can derive the equation

$$M_0 = mN \frac{e^{\frac{\Delta E}{k_b T}} - 1}{e^{\frac{\Delta E}{k_b T}} + 1} = mN \tanh\left(\frac{\Delta E}{2k_b T}\right) \quad (2.11)$$

as the argument in the hyperbolic tangent is small, the expression further simplifies to

$$M_0 \approx mN \frac{\Delta E}{2k_b T} \quad (2.12)$$

In most MR scanners, there is a strong main magnetic field applied in one direction, or, $\mathbf{B} = B_0 \hat{z}$. If this is true, we can substitute Equation 2.1 and 2.4 into equation 2.12, which gives us the expression

$$M_0 \approx N\gamma^2\hbar^2 \frac{B_0}{4k_bT} \quad (2.13).$$

One can observe that the magnetization of the sample is linearly dependent on the main magnetic field strength B_0 . The greater amount of magnetization would result in larger magnetization of the sample. MR scanners typically operate with a strong magnetic field. Even MR scanners colloquially described as "low field", such as a 0.5 T magnet, still operates at 10000x the earth's magnetic field strength.

2.1.3 - Magnetic Precession

The interaction between magnetization vector and an external magnetic field can be described classically by the differential equation[1]

$$\frac{d\mathbf{M}}{dt} = \gamma\mathbf{M} \times \mathbf{B} \quad (2.14)$$

where \mathbf{M} is the vector describing the magnetization of the sample and \mathbf{B} is the magnetic field vector. Assuming again that in the MR scanner where $\mathbf{B} = B_0\hat{\mathbf{z}}$, Equation 2.14 can be separated into 3 components, as

$$\begin{aligned} \frac{dM_x}{dt} &= \gamma M_y B_0 \\ \frac{dM_y}{dt} &= -\gamma M_x B_0 \\ \frac{dM_z}{dt} &= 0 \end{aligned} \quad (2.15)$$

The solution of these equations yields the expressions

$$\begin{aligned}
M_x(t) &= M_x(0)\cos(\omega_0 t) + M_y(0)\sin(\omega_0 t) \\
M_y(t) &= M_x(0)\sin(\omega_0 t) + M_y(0)\cos(\omega_0 t)
\end{aligned}
\tag{2.16}$$

$$M_z(t) = M_z(0)$$

If there are transverse magnetization components present, such that M_x or M_y is greater than zero, these equations describe a "spinning top" like motion known as the Larmor precession about the z axis. The frequency,

$$\omega_0 = \gamma B_0 \tag{2.17}$$

is known as the Larmor frequency. However, at the equilibrium position where $M = M_0 \hat{z}$, there are no transverse magnetization components, such that $M_x(0) = 0$, $M_y(0) = 0$, and no spin dynamic occurs. Transverse magnetization can be generated by perturbation of the system with a radiofrequency (RF) pulse, which will be described in section 2.1.6.

2.1.4 - Bloch's equation and MR Relaxation

While external perturbation causes MR magnetization to precess, the system will gradually return to thermal equilibrium. This process is known as relaxation. By adding relaxation terms to Equation 2.14 yields the Bloch's equation, given as [1]

$$\frac{d\mathbf{M}}{dt} = \gamma \mathbf{M} \times \mathbf{B} + \frac{M_x \mathbf{x} + M_y \mathbf{y}}{T_2} + \frac{M_z \mathbf{z}}{T_1} \tag{2.18}$$

In Equation 2.18, there are two separate relaxation terms describing the relaxation in transverse plane and z-direction. The middle term describes transverse, spin-

spin (T_2) relaxation, in which the individual spins interact with one another and lose coherence at a rate described by the T_2 relaxation time. The last term describes the longitudinal, spin-lattice (T_1) relaxation, a process where spins lose energy to its surrounding environment, at a rate described by the T_1 relaxation time. Separating the Bloch's equation into 3 components yields

$$\begin{aligned}\frac{dM_x}{dt} &= \gamma M_y B_0 + \frac{M_x}{T_2} \\ \frac{dM_y}{dt} &= -\gamma M_x B_0 + \frac{M_y}{T_2}\end{aligned}\tag{2.19}$$

$$\frac{dM_z}{dt} = \frac{M_z - M_0}{T_1}$$

with the solution

$$\begin{aligned}M_x(t) &= [M_x(0)\cos(\omega_0 t) + M_y(0)\sin(\omega_0 t)]e^{-\frac{t}{T_2}} \\ M_y(t) &= [M_x(0)\sin(\omega_0 t) + M_y(0)\cos(\omega_0 t)]e^{-\frac{t}{T_2}} \\ M_z(t) &= M_0 + (M_z(0) - M_0)e^{-\frac{t}{T_1}}\end{aligned}\tag{2.20}$$

2.1.5 - Rotating Frame of Reference

The equations describing MR physics can be greatly simplified if these are in a frame of reference rotating about the z-axis at the Larmor frequency. At this frame of reference there is no precession from the static field, so the effective static B_0 , or $B_{eff} = 0$, the cross product term in the Bloch equation is zero. The solutions to the Bloch equations greatly simplifies to [2]

$$\begin{aligned}M_x(t) &= M_x(0)e^{-\frac{t}{T_2}} \\M_y(t) &= M_y(0)e^{-\frac{t}{T_2}}\end{aligned}\tag{2.21}.$$

$$M_z(t) = M_0 + (M_z(0) - M_0)e^{-\frac{t}{T_1}}$$

Generally, equations describing MR signals will be expressed in the rotating frame of reference.

2.1.6 - RF (B_1) Tipping Pulse

MR magnetization within a sample can be made to precess by applying a transverse B_1 RF field to the sample. In the rotating frame of reference, the magnetization vector, \mathbf{M} can be rotated out of the equilibrium position by the application of a magnetic field B_1 in a direction orthogonal to the z-axis (i.e. the x or y direction). The angle of rotation, α by \mathbf{M} is described by the equation[2]

$$\alpha = \gamma B_1 \tau\tag{2.22}$$

where τ is the time during of RF (B_1) pulse, the rotation angle α is sometimes called the ``flip angle``. After the magnetization has rotated away from

equilibrium (i.e. z-direction in the rotating frame of reference), it undergoes precession and relaxation as described by the Bloch's equation. The transverse component of the magnetization can be detected by placing receiver coils on the one of the orthogonal orientations (i.e. x or y direction). Generally, the signal induced in the receiver coil is maximum for a flip angle of 90° . The time-dependent voltage detected by the receiver coils after the application of a single B_1 pulse is called the free-induction decay (FID).

2.1.7 - T_2 and T_2^*

After a $90^\circ B_1$ pulse is applied to a sample, one might expect the signal to decay at a rate (T_2) described by equation 2.29 and 2.30. However, the observed decay time is actually shorter than this expected value. This phenomenon is due to the local magnetic field inhomogeneity within the sample caused by small spatial variations in the B_0 field. These small differences in B_0 causes the spins to precess at slightly different Larmor frequencies, which causes the signal to decay at rate described by [2]

$$\frac{1}{T_2^*} = \frac{1}{T_2} + \gamma\Delta B \quad (2.23)$$

where T_2^* represents the shortened relaxation time, and ΔB represents local field inhomogeneity. The term $\gamma\Delta B$ is sometimes denoted as $1/T_2'$. T_2^* relaxation is therefore a combination from two different effects. T_2 arises from thermodynamic processes which are irreversible, whereas T_2' arises from inhomogeneity in the external field and magnetic susceptibility differences (basically any time-independent variation) which is reversible. The effect of T_2' dephasing can be

reversed by applying a 180° RF pulse following the 90° excitation RF pulse which leads to the formation of a ``spin-echo``.

2.1.8 - MR Signal Detection

The voltage induced in these coils can be described by Faraday`s law, which states that[2]

$$V = \frac{d\Phi}{dt} \quad (2.24)$$

where c is the speed of light, and Φ describes the magnetic flux, which is expressed as

$$\Phi = NAB_x = 4\pi NAM_x \quad (2.25)$$

in which N is the number of loops in the coil, A is the cross sectional area of the sample, and B_x and M_x are the magnetic field and magnetization in the x-direction. However, from eq.2.20 we know that M_x can be described as

$$M_x = M_T \sin(\omega_0 t) \quad (2.26)$$

Where M_T is the magnitude of the transverse component of the magnetization.

Therefore, the voltage induced in the coil is given as follows.

$$V = 4\pi NA \frac{dM_x}{dt} \quad (2.27)$$

where

$$\frac{dM_x}{dt} = \left[M_T \omega_0 \cos(\omega_0 t) + \frac{dM_T}{dt} \sin(\omega_0 t) \right] \quad (2.28)$$

The first term describes the contribution from precession (proportion to ω_0 , which is ~128 MHz for a 3 T scanner), which is many orders magnitude larger than the second term that describes the contribution from transverse relaxation (proportion to $1/T_2$ which is in the order of a few Hz for most tissues). Ignoring the 2nd term, the voltage induced in the coil is

$$V = 4\pi N A M_T \omega_0 \cos(\omega_0 t) \quad (2.29)$$

One can therefore observe that the amount of induced voltage is proportional to B_0^2 as both the net magnetization M_T and the Larmor frequency ω_0 are linearly dependent on B_0

2.2 - Imaging Principles

The previous section discussed the use of an RF pulse to tip away the net magnetization of the sample from z-axis to the transverse plane and the signal induction by the transverse magnetization within a receiver coil. However, in order to visualize anatomy in 2D or 3D images, spatial localization of MR signals must be performed.

2.2.1 - Fourier Transform

The Fourier transform is an important mathematical operation that decomposes a function into its constituent frequencies, and is also an important concept in for MR imaging. The Fourier transform is defined as follows [2]

$$f(k) = \frac{1}{\sqrt{2\pi}} \int_{-\infty}^{+\infty} dx F(x) e^{-ixk} \quad (2.30)$$

The function $F(x)$ describes the variation of image intensities in spatial domain whose Fourier transform is given by the function $f(k)$. Both functions are assumed, in general, to be complex. Conceptually, $f(k)$ is the frequency spectrum of $F(x)$. The original function $F(x)$ can be mathematically recovered from $f(k)$ by applying the inverse Fourier transform, described as,

$$F(x) = \frac{1}{\sqrt{2\pi}} \int_{-\infty}^{+\infty} dk f(k) e^{ixk} \quad (2.31)$$

Equations 2.30-2.31 are the Fourier transform pairs in 1D, but the formulations generalizes to N-dimensions with straight forward extensions.

2.2.2 - Magnetic Field Gradients

MR signals can be spatially localized by the application of linearly spatially varying magnetic fields since the Larmor frequency is linearly proportional to the total magnetic field at a point. An MR imaging devices typically contain a set of gradient coils capable of generating linear magnetic field gradient in 3 orthogonal directions. The effect of magnetic field gradients can be mathematically described as [2]

$$\Delta B(x, y, z) = \mathbf{r} \cdot \mathbf{G} = xG_x + yG_y + zG_z \quad (2.32).$$

where ΔB is the additional magnetic field strength at (x, y, z) due to the application of linear gradient, the vector \mathbf{r} describes the position within the field,

and \mathbf{G} is magnetic field slope vector, also known as gradient strength. It is worth nothing that while the gradient field ΔB varies in the 3 orthogonal directions, the direction of ΔB is in the z direction, parallel to B_0 . Combining the main field to the gradient field yields the expression

$$\mathbf{B}(\mathbf{r}) = \hat{\mathbf{z}}(\mathbf{r} \cdot \mathbf{G} + B_0) \quad (2.33).$$

2.2.3 - Slice Selection

In tomographic imaging, one of the three spatial dimensions is usually localized by selecting a slice (i.e. 2D plane) or a set of slices to be imaged. In MR imaging, this is achieved through the application of a slice selective pulse in conjunction with gradients in any desired direction. A slice selective gradient can be applied such that the magnetization in a plane within the sample, perpendicular to vector \mathbf{G} , will precess at the same Larmor frequency. The RF (B_1) pulse, typically a sinc pulse in the time domain, is used because, the Fourier transform of the sinc pulse of time, in the frequency domain is a rectangular function. The width of the rectangular function is related to the slice thickness, described by the expression

$$d = \frac{\Delta\omega}{\gamma G} \quad (2.34)$$

in $\Delta\omega$ is also known as the frequency bandwidth, the difference between the maximum and the minimum frequency slice. In principle, slice selective excitation can be applied in 3 orthogonal directions to achieve spatial localization of volume element (voxel) for imaging. However, this is a highly inefficient

method of data collection, and faster methods of encoding the remaining two dimensions within the selected plane are generally used.

2.2.4 - Frequency Encoding and Quadrature Detection

If a magnetic field gradient is applied in a direction (e.g. x-direction) orthogonal to the slice selective direction (e.g. z-direction) during acquisition, the detected time domain FID will contain a range of frequencies. With the gradient G applied in the x-direction, the magnetization in the x-direction of the selected plane will precess at a range of frequencies. In particular, the Larmor frequency at x is $\omega_0 + \gamma xG$, and the voltage induced is given as follows.

$$V(t) = \int dx P(x) \cos(\omega_0 + \gamma xG) t \quad (2.35)$$

where $P(x)$ is the projection of 2-D magnetization of the selected plane in the x-direction. In quadrature detection, this induced voltage is split into two components each obtained by multiplication with a reference signal oscillating at the natural Larmor frequency. The reference signals of the two components are 90° out of phase with one other as

$$\begin{aligned} V_1(t) &= V(t) \cos(\omega_0 t) \\ &= \int dx P(x) [\cos(2\omega_0 + \gamma xG) t + \cos(\gamma xG)] t \end{aligned} \quad (2.36)$$

$$\begin{aligned} V_2(t) &= V(t) \sin(\omega_0 t) \\ &= \int dx P(x) [\sin(2\omega_0 + \gamma xG) t - \sin(\gamma xG)] t \end{aligned} \quad (2.37)$$

For each of two signal components, the high frequency component of the signal is removed by means of a low-pass filter.

$$V_1(t) = \int dx P(x) \cos(\gamma x G t) \quad (2.38)$$

$$V_2(t) = \int dx P(x) \sin(\gamma x G t) \quad (2.39)$$

The two components are generally described as the “real” and “imaginary” component of the detected signal. The two 90° out of phase signals allow one to distinguish whether the frequency is positive or negative. The combination of the two signals is a generally a complex signal given as follows.

$$C(t) = V_1(t) - iV_2(t) \quad (2.40)$$

which can be expressed as

$$C(t) = \int dx P(x) e^{i\gamma x G t} \quad (2.41).$$

By making the substitution $k = \gamma G t$ in Equation 2.41, one get the expression

$$C(k) = \int dx P(x) e^{ikx} \quad (2.42)$$

A simple application of a inverse Fourier transform in eq.2.42 one can recover the spatially localized signal

$$P(x) = \frac{1}{2\pi} \int dk C(k) e^{-ikx} \quad (2.43).$$

In summary, in frequency encoding, a magnetic field gradient is applied during data acquisition. Spatial information is recovered by the inverse Fourier transform of the resulting quadrature detected signal.

2.2.5 - Phase Encoding

From Equation 2.41, we can extract the important physical quantity

$$\phi = \gamma x G t \quad (2.44)$$

which is known as phase. Spatial information in the direction orthogonal to the frequency encoding direction can be localized by manipulating the phase of the magnetization with the selected plane. This process is known as phase encoding process that varies the phase along the phase encoding direction (i.e. y-direction) by the application of another linearly varying gradient.

For simplicity, let us say that the total magnetization is to be spatially localized at 3 different points, $-y$, 0 , y , with an associated magnetization of m_{-y} , m_0 and m_y , at these points, respectively. In order to achieve this, 3 spatial encoding steps, with y-direction gradients of magnitudes, $G_y = -g$, 0 and g are applied after the slice selective z-gradient, but prior to frequency encoding needed for data acquisition. The phase can be determined by eq. 2.44. In the first experiment, the encoding gradient g will create the phase of $\phi = -\theta$, 0 , and θ , where $\theta = \gamma y g T$, for m_{-y} , m_0 and m_y . The projection from the first experiment is

$$p_{+g} = m_{-y} e^{-i\theta} + m_0 + m_y e^{i\theta} \quad (2.45)$$

The 2nd experiment, there is no phase, the projection is therefore simply

$$p_0 = m_{-y} + m_0 + m_y \quad (2.46)$$

For the 3rd experiment, the gradient of $-g$, the projection is

$$p_{-g} = m_{-y}e^{i\theta} + m_0 + m_ye^{-i\theta} \quad (2.47)$$

We can define the matrix notations

$$\mathbf{F} = \begin{bmatrix} e^{i\theta} & 1 & e^{-i\theta} \\ 1 & 1 & 1 \\ e^{-i\theta} & 1 & e^{i\theta} \end{bmatrix} \quad (2.48)$$

$$\mathbf{m} = \begin{bmatrix} m_g \\ m_0 \\ m_{-g} \end{bmatrix} \quad (2.49)$$

$$\mathbf{p} = \begin{bmatrix} p_g \\ p_0 \\ p_{-g} \end{bmatrix} \quad (2.50)$$

Equations 2.45-2.47 can be written in matrix form

$$\mathbf{P} = \mathbf{F}\mathbf{m} \quad (2.51)$$

The goal is to recover the spatially localized matrix \mathbf{m} from the acquired projections \mathbf{P} , by using an inverse matrix

$$\mathbf{m} = \mathbf{F}^{-1}\mathbf{P} \quad (2.52)$$

Three phase encoding gradient steps is not sufficient to generate acceptable images. The typical number of phase encoding steps in MR imaging are 2^N numbers such as 64, 128, 256, 512. The phase encoding gradients are chosen that

the phase increases linearly from negative maximum to positive maximum in a step-by-step manner. In an example where 256 phase encode is used, The elements of the matrix F is defined as

$$F_{jk} = \frac{1}{\sqrt{256}} e^{-i\frac{2\pi jk}{256}} \quad (2.53)$$

The matrix F and inversion matrix F^{-1} is the forward and inverse discrete Fourier transforms operators. The spatially localized signal (image) is a 2D inverse Fourier transform of the series of projections.

2.3 - Spin Echo based Imaging Sequences

2.3.1 - Spin Echo Sequence

This section introduces several basic MRI sequences. As noted previously, an FID signal from a 90° pulse leads to T_2^* related signal losses caused by magnetic field inhomogeneities. However, this loss is recoverable by a sequence known as the spin-echo experiment. In the spin echo experiment, the 90° excitation pulse is followed by a 180° refocusing pulse after a time t . The polarity of phase is reversed, and the inhomogeneity that caused spins to de-phase now causes the spins to go back in phase. At precisely $2t$, or the echo time (TE), the phase coherence is again at maximum, and the signal formed from this is called an echo. However, the de-phasing from spin-spin interaction (T_2) is not recoverable. If only one re-focussing pulse is performed, the signal dependence on TE is given as follows[2],

$$S(TE) = M_0 e^{\frac{-TE}{T_2}} \quad (2.54)$$

where M_0 is the theoretically attainable maximum signal which is directly proportional to Eq 2.28. As multiple excitations (with different phase encode gradients) are required to generate an image, transverse relaxation (T_1) effects also come into play. Prior to the initial excitation, M_z is at its maximum point at thermal equilibrium. A 90° pulse flips the magnetization onto the x-y plane, and $M_z = 0$. T_1 relaxation occurs between timing interval between consecutive excitation pulses, known as the repetition time (TR). T_1 and TR determines how quickly the M_z magnetization will recover and be available for the next excitation. Eventually, a steady state level of M_z is achieved for the start of each excitation. The amount of signal available is described by

$$S(TE, TR) = M_0 \left(1 - 2e^{-\frac{-(TR - \frac{TE}{2})}{T_1}} + e^{-\frac{TR}{T_1}} \right) e^{\frac{-TE}{T_2}} \quad (2.55)$$

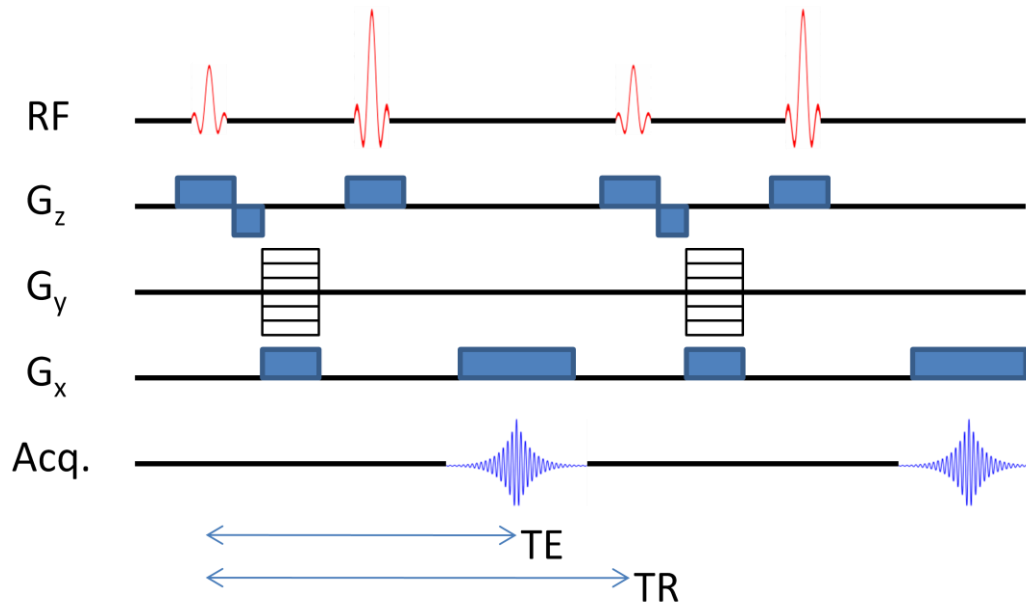


Figure 2-1: Sequence diagram for a spin echo sequence. RF describes the radiofrequency pulse, G_x, G_y, G_z describes the x, y, z gradients, and Acq. describes the acquired signal. TE is the echo time, and TR is the repetition time.

While T_1 and T_2 values are inherent to the MR sample, TE and TR times are

parameters chosen by the user of the MRI. T_2 relaxation effects are minimized

when $TE \ll T_2$, while T_1 relaxation effects are minimized when $TR \gg T_1$.

However, increasing TR will increase scan time, while hardware limits, such as the gradient strength of the system, will limit how short the TE can be chosen.

2.3.2 - Multiple Spin Echo Sequence as a T_2 Measurement Tool

If images can be acquired with several different TE s, while maintaining the same

TR, the measured signal can be used to measure the T_2 of the MR sample. A T_2

relaxation curve described by Eq. 2.53 can be generated, and exponential fitting

allows for the determination of T_2 . In principle, several spin-echo experiments

can be performed to acquire the necessary data, but it is time consuming as spin

echo sequence is a relatively slow sequence. A more efficient method of data

collection is the multi-spin echo approach – in which multiple 180 refocusing pulses follow a single excitation pulse to acquire data for multiple images with different TE . A dual-echo example is shown in Figure 2-2. in which two full images will be acquired at echo times of TE_1 and TE_2 . This approach can be further extended to acquire many more images with different TE (i.e. the CPMG sequence[3]) for a more accurate determination of T_2 .

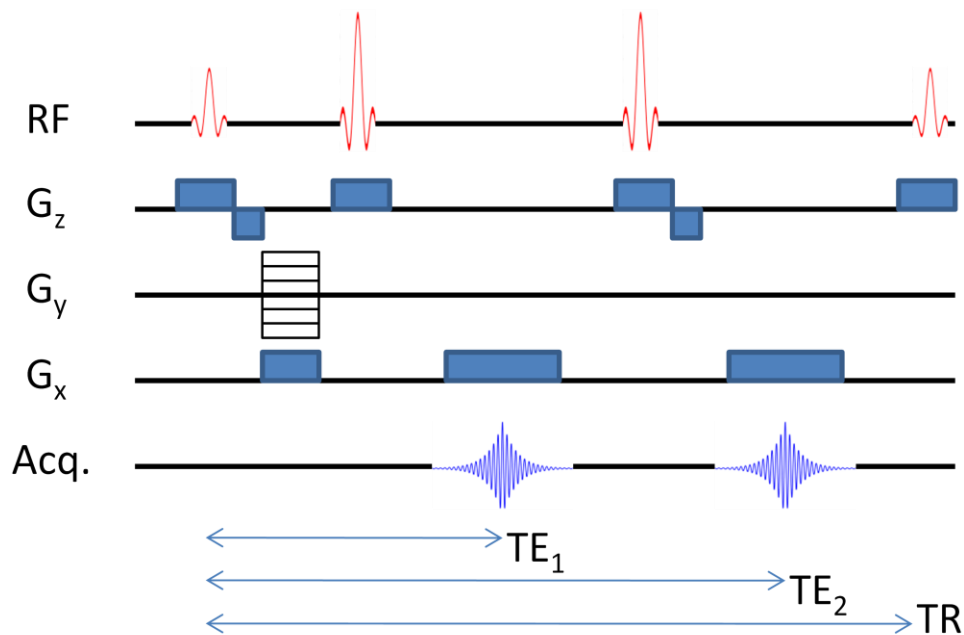


Figure 2-2: Sequence diagram for a multi-spin echo sequence.

2.3.3 - Inverse Recovery Sequence as a T_1 Measurement tool

One can also determine T_1 from the spin echo approach (Equation 2.55). TE will be fixed while TR is varied, and the signal measured can be fitted to the equation

$$S(TR) = S(0) \left(1 - e^{-\frac{TR}{T_1}} \right).$$

However, a more accurate measurement of T_1 is usually obtained with an inverse recovery sequence that leads to a special type of contrast in MR images. In an inverse recovery sequence, a 180° inversion pulse is

first applied at an inversion time, TI prior to the standard spin echo sequence of a 90° excitation pulse followed by the 180° refocusing pulse, as shown in Figure 2.3. After the inversion pulse, M_z is oriented towards the negative-z direction and begins to relax towards the positive z direction. The chosen TI time will determine the amount of initial magnetization available for the initial excitation. This addition IR pulse yields the signal contrast

$$S(TI, TE, TR) = M_0 \left(1 - 2e^{-\frac{TI}{T_1}} + e^{-\frac{TR}{T_1}} \right) e^{-\frac{TE}{T_2}} \quad (2.56)$$

For measuring T_1 , several images are acquired with different TI , while TE is fixed. The repetition time TR is chosen to be long enough such that $e^{-\frac{TR}{T_1}}$ term is approximately 0. The signal measured is then fitted to the equation $S(TI) = S_0 \left(1 - 2e^{-\frac{TI}{T_1}} \right)$ in order to extract T_1 . The wider dynamic range of this curve leads to more accurate measurements of T_1 . It should be noted that there is a special inversion time known as a null point ($TI = 0.69 T_1$) in which the signal will be completely eliminated. This can be useful to suppress signals from certain types of tissues, such as fat.

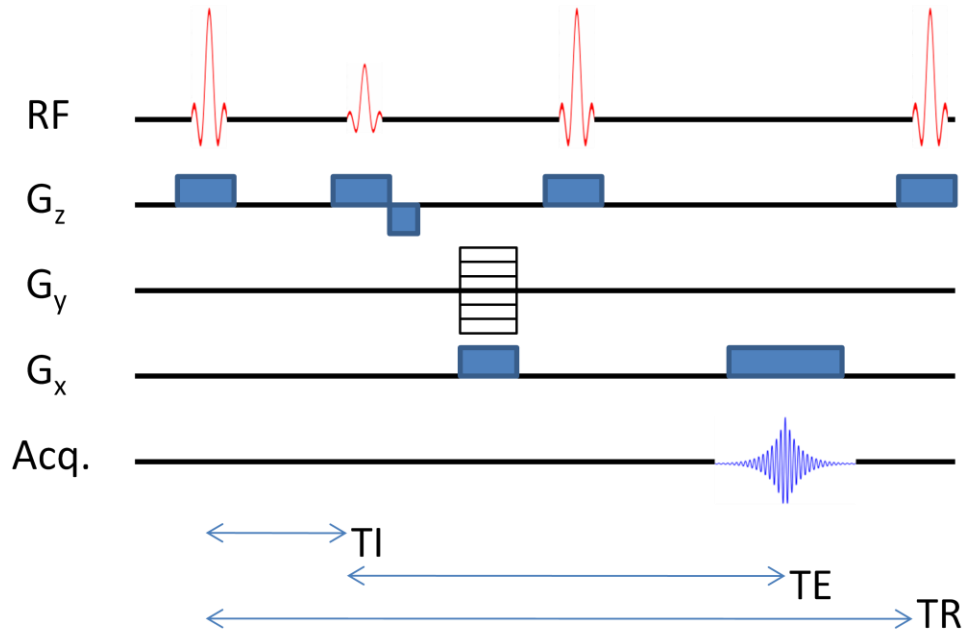


Figure 2-3: Sequence diagram for an inverse recovery sequence.

2.3.4 - Turbo Spin Echo Sequences

The idea behind the multiple spin echoes method, in which multiple 180 refocusing pulses follow a single excitation pulse to create multiple images for various TE values, can also be used to speed up acquisition of a single image, by acquiring multiple phase encode with a single excitation pulse. This approach is known as the turbo spin echo (TSE) approach. This sequence has different names among different vendors including the Fast Spin Echo (FSE) or Rapid Acquisition with Relaxation Enhancements (RARE). This sequence acquires the FID of each phase-encode with a different TE value. Therefore, the relationship of pixel values and relaxation time is not simple[2]. However, in applications where quantitative information about relaxation times is not important, TSE sequence offers high quality SE like images while significantly reducing the imaging time

2.4 - Gradient Echo Imaging

2.4.1 - FLASH Sequence

To further increase imaging speed, a whole family of gradient echo based sequences has been developed. In a gradient echo sequence, only RF excitation pulses of a specified angle is used in a fixed interval of time (TR). The magnetization undergoes relaxation before the next excitation. After some initial pulses, the system gradually reaches a steady state in which each RF pulse produces the same amount of magnetization in the transverse plane. Instead of refocusing pulses, echoes are formed by the de-phasing and rephasing of spins by the frequency encoding gradient. As there is no 180° refocusing, the T_2' effect is not reversed. As a result, gradient echo sequence is T_2^* weighted rather than T_2 weighted. A version of the FLASH sequence with gradient spoiling is shown in Figure 2-4. RF pulses with phase cycling are another means to achieve spoiling. The purpose of spoiling is to remove the remaining transverse signal at the end of each excitation to create T_1 weighting. This sequence is also known as SPGR and T_1 -FFE, and the sequence diagram is shown in Figure 2-4. The signal acquired in the FLASH sequence is described by the expression[3]

$$S = \frac{M_0 \sin \theta (1 - e^{-TR/T_1})}{(1 - \cos \theta e^{-TR/T_1})} e^{-\frac{TE}{T_2^*}} \quad (2.57)$$

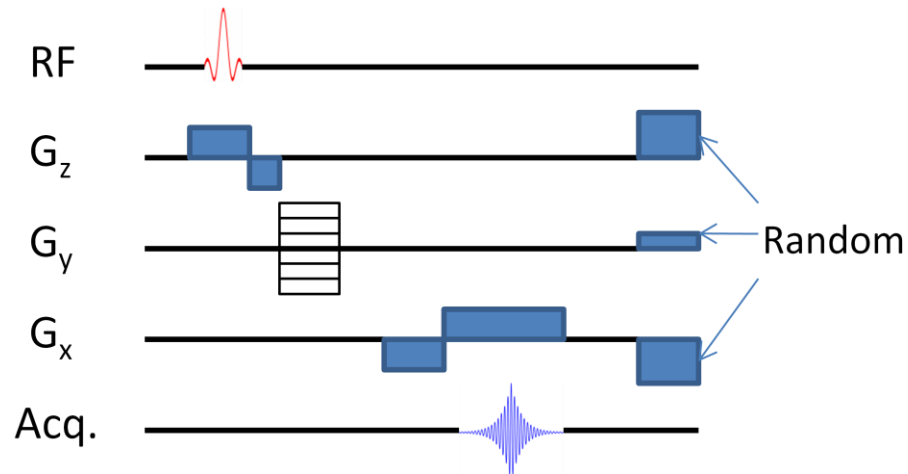


Figure 2-4: Sequence diagram of the FLASH sequence. Random gradients are employed to spoil the remaining transverse magnetization at the end of each TR interval.

The speed of gradient echo sequences can be significantly enhanced by combining a small flip angle and a much shorter TR. When TR is short, a 90° pulse will not provide maximum signal, as there is not enough time for the longitudinal component to recover. An optimal flip angle to generate maximum signal is known as the Ernst angle[3], described by

$$\alpha_{opt} = \arccos \left(e^{\frac{-TR}{T_1}} \right) \quad 2.58$$

2.4.2 - SSFP-FID and SSFP-Echo

An unspoiled, steady state free precession (SSFP) sequence provides a greater amount of signal available than FLASH[3]. A necessary condition for SSFP is a re-winder phase encoding gradient. Two separate signals can be created from SSFP. The SSFP-FID is formed from the FID of each excitation pulse. On the other hand, the SSFP-echo, a time reversed FID, that appears before each excitation pulse due to the refocusing effect of consequence RF pulses. An example of SSFP-FID and SSFP-echo sequence is shown in Figures 2-5

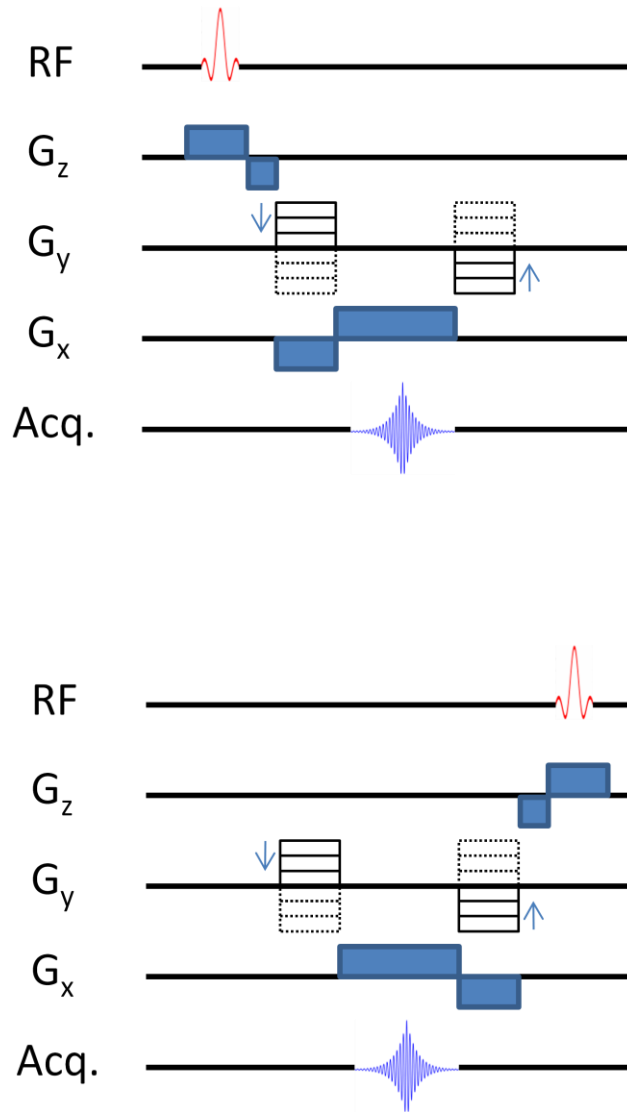


Figure 2-5: Sequence diagram for the SSFP-FID sequence (Top) and the SSFP-echo sequence (Bottom). They are mirror image of each other

2.4.3 - Balanced SSFP

Balanced SSFP (bSSFP) incorporates a SSFP sequence in which the net gradient area on any axis is zero in each TR interval, as shown in Figure 2-6. The signal peak from the SSFP-FID and the SSFP-echo will coincide with each other to create a signal that is a coherent sum of the two separate signals. Thus a signal

large in magnitude is produced compared to the other SSFP sequences. The signal of a bSSFP sequence can be expressed as [3]

$$S = M_0 \sin\theta \frac{1 - E_1}{1 - (E_1 - E_2) \cos\theta - E_1 E_2} e^{-\frac{TE}{T_2}} \quad (2.59)$$

Where E_1 and E_2 are equal to $e^{-\frac{TR}{T_1}}$ and $e^{-\frac{TR}{T_2}}$ respectively. In cases where $TR \ll T_2$, the equation simplifies to

$$S = \frac{M_0 \sin\theta}{T_1/T_2 (1 - \cos\theta) + (1 + \cos\theta)} e^{-\frac{TE}{T_2}} \quad (2.60)$$

Due to the T_1/T_2 term in the denominator, bSSFP is often described to have T_2/T_1 contrast weighting. Also, one can observe from the term “ $e^{-\frac{TE}{T_2}}$ ” that the bSSFP sequence is T_2 weighted rather than being T_2^* weighted [3]. Proof of T_2 weighting was demonstrated by Scheffler and Hennig [4] for cases where $TE = TR/2$, a condition satisfied in most applications of bSSFP. The optimal flip angle for maximum signal for bSSFP is [3]

$$\theta_{max} = \arccos\left(\frac{T_1 - T_2}{T_1 + T_2}\right) \quad (2.61)$$

Another important property of this sequence is the presence of banding artefacts. Local field inhomogeneity creates unwanted phase to be accumulated during each TR cycle. A low signal region (a band) occurs when the accumulated phase is

180°. As phase accumulation is proportion to TR , shorter TR is an effective way to reduce TR . BSSFP sequence is inherently more suitable for lower field imaging, this is because local field inhomogeneity is much more severe at higher magnetic fields.

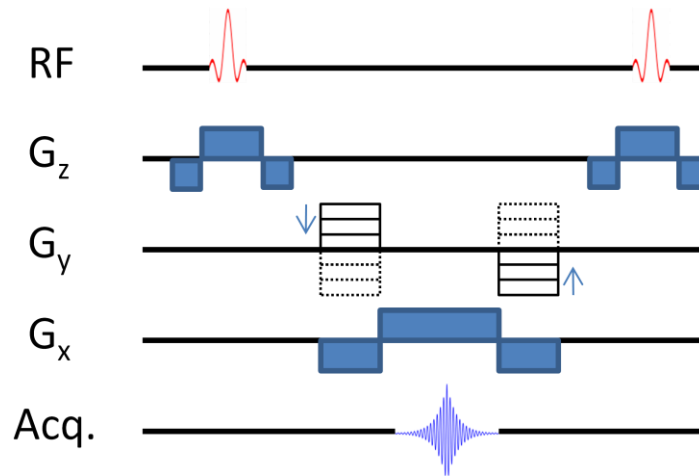


Figure 2-6: Sequence diagram for the balanced SSFP sequence.

2.5 - Signal, Noise, and Contrast

2.5.1 - Signal-to-Noise Ratio

The discussion in the previous sections was confined to the magnitude of the MRI signal available in each of the MRI sequences. However, the presence of noise in the acquired signal is an important factor as the noise in the data propagates as noise in the MR images. Large fluctuations in MRI images are detrimental to the image quality. Noise in the acquired FID arises from Brownian motion of electrons in a conductor, which is also known as resistance noise[1]. Noise arises from both resistance in the coil and the imaged sample. In the presence of such noise, an important indicator of image quality is the signal to noise ratio (SNR) defined as follows.

$$\text{SNR} = \frac{\text{Signal Amplitude}}{\text{standard deviation of noise}} \quad (2.62)$$

where the ‘signal magnitude’ is usually the mean pixel intensity of a region of interest in the image, and the standard deviation of noise is measured by calculating the standard deviation in a region of the image with uniform signal. Recall that in quadrature detection, MR signal is a complex quantity with real and imaginary components required for Fourier transform. After Fourier transform, complex images with real and imaginary components are generated. While real and imaginary images have little physical meaning individually, they can be combined to calculate magnitude and phase images. The scalar magnitude images are the images most commonly used in clinical MRI. However, one must be careful in measuring noise from the magnitude images. Due to the manner in which magnitude signal is calculated, the noise in the magnitude images follows a probability distribution resembling a Rician distribution (non-negative). If noise is measured in the magnitude images of a uniform phantom in regions where $\text{SNR} > 2$, the Rician and Gaussian distributions are approximately equal and no correction would be needed [5]. As patients are generally non-uniform, the noise would be best measured in a region outside the patient image where there is no signal. In such instances ($\text{SNR} < 2$), the Rician distribution becomes a Rayleigh distribution, and the measured standard deviation will not be representative of the noise in the high SNR region of interest within the patient image. A correction factor, thus, must be applied. The noise characteristics for phased array coils are more complicated, and are beyond the scope of this work.

The problem of noise bias can be avoided if noise is measured in a zero signal region in the real or imaginary images where negative values are allowed.

The overall SNR depends on many factors, which can be summarized in the following equation[1]

$$SNR \propto \Delta x \Delta y \Delta z \sqrt{\text{total readout interval}} f(\rho, T_1, T_2) \quad (2.63)$$

where, Δx , Δy , Δz , represents the voxel dimension, the readout interval term describes the number of excitations and the number of encoding steps on each dimension, and the $f(\rho, T_1, T_2)$ is a sequence dependent function, such as eq. 2.53 for spin echo images, eq.2.57 for FLASH and eq. 2.59 for bSSFP sequences. The proton density term ρ is built into M_0 in those equations.

2.5.2 - Contrast to Noise Ratio

The key objective in many applications of MR imaging is to distinguish between diseased and healthy tissues. The difference in signal between two types of tissue is known as contrast. This signal difference will also be degraded by the presence of MR noise. The concept of contrast to noise ratio (CNR) is thus introduced as a quantitative measure of image quality. Assuming uniform noise over the imaging field of view, CNR is defined as

$$\begin{aligned} \text{CNR} &= \frac{\text{Signal Difference}}{\text{standard deviation of noise}} \\ &= \Delta SNR \end{aligned} \quad (2.64).$$

In the context of lung tumour tracking, CNR is an important quality that describes the ability to distinguish a lung tumour from healthy lung parenchyma tissues in the presence of imaging noise. Tumour and normal tissues may exhibit differences in ρ , T_1 and T_2 , giving rise to differences in SNR (eq. 2.63).

2.6 - Effects of Changing Main Magnetic Field Strength

2.6.1 - SNR Dependence on B_0

The effect of varying the main magnetic field strength (B_0) on image quality is an important aspect of this thesis. Eq. 2.29 shows that the induced voltage in an MR experiment is proportional to both the magnetization and the precession frequency which, in turn, are both linearly proportional to B_0 (Eqs. 2.13 and 2.17). Thus the MR signal is proportional to B_0^2 . However, MR noise also depends on B_0 , but in a more complex manner. MR noise, as previously described, comes from two sources: resistance from the coil; and resistance from the body. Noise arising from the body has been shown to be proportional to B_0 , whereas noise arising from the coil is known to be proportional to $B_0^{\frac{1}{4}}$ [1]. If either coil noise or body noise is dominant, the relationship between SNR and B_0 can be simplified to approximately

$$SNR \propto B_0 \tag{2.65}$$

$$SNR \propto B_0^{\frac{7}{4}} \tag{2.66}$$

where expression 2.65 represents the SNR relation when resistance from the body is the dominant factor, while equation 2.66 represents the relationship when coil

resistance is the dominant effect. In typical MR coils used for imaging patients, for field strength less than 0.2 T, coil noise dominates and equation 2.66 is used to estimate the relationship between SNR and B_0 ; whereas for field strengths greater than 0.2 T, body noise dominates effect and equation 2.65 is used to estimate the relationship between SNR and B_0 [6]. For example, going from 3 T to 0.5 T would mean a reduction of SNR by a factor of 6. These relationships are often used to justify the modification of an image acquired at a higher field strength to simulate an image acquired at lower field. SNR can be downgraded by the addition of zero mean Gaussian noise. This process does not modify the signal but increases noise, resulting in a reduction of SNR and CNR. The previous example of scaling from 3 T to 0.5 T will suggest that the noise be amplified by a factor of 6. This process will be described in this work as *linear SNR/CNR scaling* to B_0 .

Expressions 2.65 and 2.66 do not account for any potential changes in relaxation times of a tissue when the main magnetic field is lowered. This issue is described in details in the next section.

2.6.2 - Relaxation Values Dependence on B_0

T_1 relaxation time is known to be dependent on B_0 , while T_2 is known to be relatively independent of it. MR relaxation is largely caused by fluctuating magnetic fields at the sites of nuclear spins. The spectral density $J(\omega_0)$ function that defines the probability that a spin system is precessing at a given ω_0 , is one way of describing the rate of these fluctuations. In systems where the fluctuations are rapid such as the case of liquid water, the spectral density is broad, whereas in

systems where the fluctuations are very slow (such as water molecules bound in very tight spaces), the spectral density is narrow[7]. Most tissues are within the intermediate region between these two extremes. Sample spectral density curves are shown in Figure 2-7.

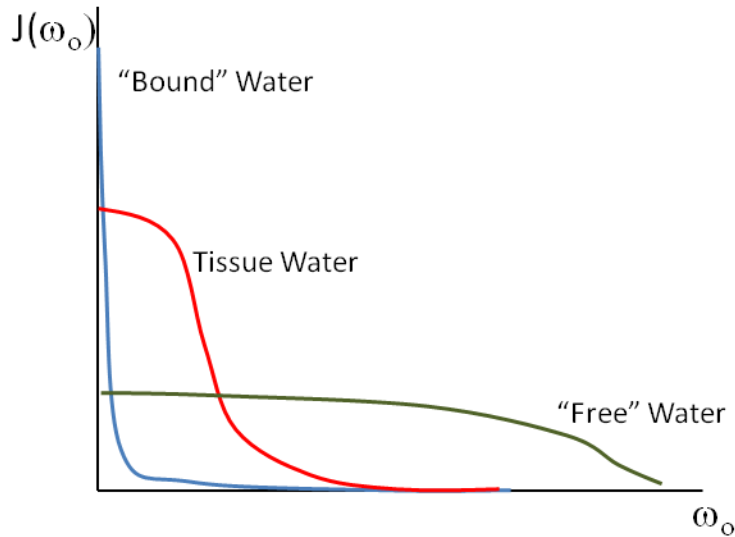


Figure 2-7: Sample spectral density for protons in 3 different environments. Blue curve represents protons in a tightly bound environment, green curve represents protons in free water, and the red curve represents water in most tissues, which is an intermediate between the other two extreme cases

T_1 and T_2 relaxation can be calculated from these spectral density curves using the Solomon equations as follows[7]

$$\frac{1}{T_1} = \text{const} * [J(\omega_0) + 4J(2\omega_0)] \quad (2.67)$$

$$\frac{1}{T_2} = \text{const} * [3J(0) + 5J(\omega_0) + 2J(2\omega_0)] \quad (2.68)$$

When B_0 is increased, the Larmor frequency will increase proportionally. The spectral density function has a lower value at higher frequency, which leads to an

increase in T_1 . For T_2 relaxation, however, the effect is much less pronounced, because of the presence of the term $J(0)$ which is independent of frequency. In tissue relaxation studies with varying B_0 , T_1 is generally modelled with the function[8]

$$T_1(\omega_0) = a\omega_0^b \quad (2.69)$$

where ω_0 is the Larmor frequency which scales linearly with B_0 . Constants a and b differ for each on types of tissues, and T_2 is generally assumed to be constant[8]. T_2^* , as described previously, is dependent on local field inhomogeneity. In some type of the tissues, such as the lung parenchyma, the magnetic susceptibility gradients between air and tissue are the main sources of local magnetic field inhomogeneity. The magnetic field inhomogeneity will scale with B_0 as follows.

$$\Delta B = \Delta\chi B_0 \quad (2.70)$$

In these type of tissues, the local susceptibility differences $\Delta\chi$ are significant, and increasing the field strength would have the effect of shortening T_2^* relaxation times. The dependence of relaxation values on field strength means that the eqs. 2.65 and 2.66 do not completely describe the relationship between SNR and B_0

2.6.3 - Specific Absorption Ratio

Energy deposition from RF pulses (RF heating) is a significant issue in high speed imaging. RF safety limits will place restrictions on scan parameters (such as flip angle) at a given imaging speed. The amount of RF energy absorbed is characterized by the specific absorption rate (SAR), which is related to B_0 as follows[3].

$$SAR \propto B_0^2 \theta^2 \Delta f \quad (2.71)$$

where θ is the flip angle and Δf is the RF bandwidth. SAR is a significant problem for fast imaging in higher field strengths.

2.6.4 - CNR

CNR is the difference in SNR between two type of tissues. The relaxation values for the two tissue types may show a different dependence with B_0 . Unless these relaxation times are accounted for, there is no simple relationship between CNR and field strength. For example, one may aim to estimate the 0.5 T CNR between two types of tissues: tissue A (T_1 at 0.5 T = 500 ms, T_1 at 3 T = 1000 ms), and tissue B (T_1 at 0.5 T of 800ms at 0.5 T, T_1 at 3 T = 1200 ms) but only a 3 T scanner is available. If the image is acquired at 3 T and linear CNR scaling is applied, the resulting image will not have the correct 0.5 T CNR - this is because signals for both tissues are underestimated due to longer T_1 at 3 T. The degree of signal under-estimation is also different for tissue A and B depending on which sequence is used. However, if one then builds a phantom that contains simulated

tissue A, that has a 3 T T_1 of 500 ms and simulated tissue B with a 3 T T_1 of 800 ms, and noise is added for linear CNR scaling, the resulting image will have the correct 0.5 T CNR because the change of relaxation times has already been accounted for in the phantom fabrication

2.7 - References

1. Nishimura DG, Principles of Magnetic Resonance Imaging, 1996
2. Xiang QS, University of British Columbia Physics 542 Notes, 2007
3. Bernstein MA, King KF, Zhou XJ, *Handbook of MRI pulse sequences*, Academic Press, 2004.
4. Scheffler K and Hennig J. Is TrueFUSP a gradient-echo or a spin-echo sequence? *Magnetic Resonance in Medicine* 49:395, 2003
5. Gudbjartsson H and Patz S. The Rician Distribution of Noisy MRI Data. *Magnetic Resonance in Medicine*, 34(6):910, 1995
6. Redpath PW, Signal-to-noise ratio in MRI. *British Journal of Radiology* 71:704, 1998.
7. Levitt MH, *Spin Dynamics: Basics of Nuclear Magnetic Resonance* John Wiley and Sons, West Sussex, England, 2008.
8. Bottemley PA, Hardy CJ, Argersinger RE and Allenmoore G, A Review of H-1 Nuclear-Magnetic-Resonance Relaxation in Pathology - Are T1 and T2 Diagnostic? *Med. Phys.* 14:1, 1987

Chapter 3 A MR Lung Contrast Phantom

3.1 - Overview

CNR is an objective and important indicator of whether a tumour can be successfully contoured, manually or automatically, in an image. It is therefore an important parameter that assesses the images acquired by the MRI integrated in a Linac-MR system. This chapter describes the theoretical rationale, design and manufacturing of lung contrast phantom that replicates the MRI contrast parameters for the lung tumour and healthy lung tissues at low magnetic field in a high-field MRI system. Contrast parameters of importance include relative proton density (PD), T_1 and T_2 .

3.1.1 - Relative Proton Density

PD difference is one of the main sources of lung tumour contrast in MR images. Healthy lung parenchyma tissue contains a significant amount of air in the alveoli and bronchioles. Therefore, the macroscopic tissue in lung parenchyma is characterized by significantly reduced water proton density compared to lung tumour and other thoracic organs. As a result, lung parenchyma often generates significantly lesser MRI signal compared to other tissues. Investigation by [1] *et al*[1] has found that PD for lung parenchyma is approximately in the range 0.2-0.35 relative to the muscle tissue. On the other hand, the water content of solid lung tumours is significantly higher. Schmidt *et al*'s[2] investigation of the lung tumour proton density has reported that that lung tumour itself has a very similar relative PD (PD = 1.04) to the muscle tissue. As a result, the PD of the

lung parenchyma relative to tumour tissue is approximately in the range of 0.19-0.34.

3.1.2 - T_1 Relaxation Times for Lung Tumour and Tissue

The T_1 relaxation times for various normal tissues and tumours have been measured at various magnetic field strengths and reported in the MR literature. Bottemley *et al*[3] collected these data from the literature and fitted them in the model shown in equation 2.69, which is $T_1(\omega_0) = a\omega_0^b \pm SD$, where SD is the standard deviation of $T_1(\omega_0)$. For healthy lung parenchyma, constants a and b were reported to be 0.00407 seconds/Hz and 0.2958 respectively, with an SD of 19%. For lung tumours, the constants a and b were found to be 0.000677 second/Hz and 0.3954 respectively, with an SD of 51%. Using these values of the fitting parameters, the increase in T_1 as a function of magnetic field strength can be shown as in Figure 3-1.

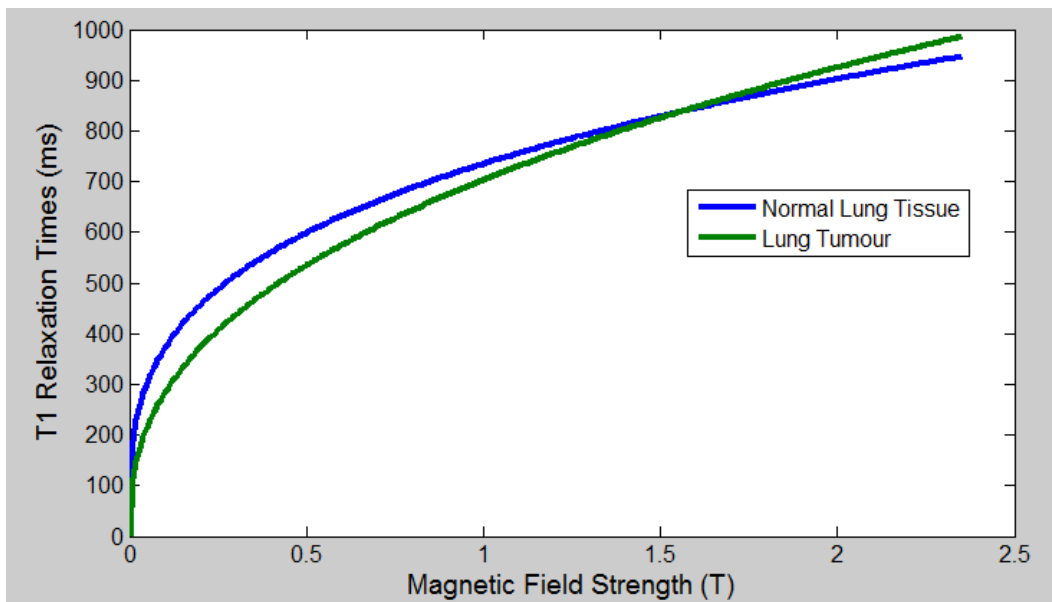


Figure 3-1: T_1 dependence on magnetic field strength for normal lung tissue and lung tumours.

Thus, the calculated values of T_1 for normal lung parenchyma and lung tumour are expected to be 455 ± 86 ms and 372 ± 185 ms, respectively, at 0.2 T, At 0.5 T, the T_1 values are 599 ± 114 ms and 532 ± 271 ms for normal parenchyma and tumour respectively. In the point of view of T_1 alone, the more rapid relaxation will offer a relative signal enhancement at lower fields in steady state. Also, the larger difference in T_1 values between tumour and normal lung tissue may provide image contrast benefit at the lower magnetic field strengths.

3.1.3 - T_2 and T_2^* Relaxation Times for Lung Tumour and Tissue

T_2 relaxation is known to be relatively independent of the main magnetic field strength in magnetic resonance experiments. Bottemley *et al* [3] report that the average measured T_2 values in the literature for lung parenchyma and lung tumour is quite similar at 79 ± 29 ms and 68 ± 45 ms respectively. The difference in T_2 is small compared to the uncertainty of these values. Therefore T_2 difference is unlikely to contribute to contrast between lung tumour and tissues. T_2^* for normal lung parenchyma is known to be significantly shorter compared to the tumour due to the T_2' effect that arise from susceptibility gradients at the air-tissue interfaces[4]. The T_2' effect is known to be stronger at higher fields[5]. This means that T_2^* contrast may be greater at higher fields strengths for some sequences.

3.2 - Materials and Methods

3.2.1 - Phantom Materials for Simulated Tissues

The idea of creating specific tissue-equivalent MR phantom is not new; MR phantoms have been created that simulate relaxation and dielectric properties of various tissues in the body at 1.5T[6]. Our phantom consists of three types of simulated tissues: lung tumour, healthy lung parenchyma, and tissues from the remaining thoracic anatomy.

3.2.1.a - Lung Tumour

For the simulated tumour tissue, the desired material should have high proton density and specific T_1 and T_2 relaxation time. The tumour is therefore made with a shaped container filled with an aqueous solution of MR contrast agents. Two types of contrast agents are available: Manganese (II) Chloride (MnCl_2 , Sigma Aldrich) and copper sulphate pentahydrate ($\text{CuSO}_4 \cdot 5\text{H}_2\text{O}$, Fischer Scientific). The cation Mn^{2+} is known to be a weak T_1 shortening agent and a strong T_2 shortening agent, whereas the Cu^{2+} has approximately similar shortening effects on T_1 and T_2 . However, in the presence of a strong T_2 shortening agent like Mn^{2+} , we found that the relative T_2 shortening effect of Cu^{2+} is effectively small, leaving it as a primarily T_1 shortening agent. Our approach is to first add MnCl_2 for the desired T_2 , and if required, subsequently add cupric sulphate to achieve the desired T_1 level. However, we experimentally determined that MnCl_2 alone can achieve approximately desired level of T_1 and T_2 relaxation times. The concentrations by volume of 0.020 g/L and 0.016 g/L of

MnCl₂ in de-ionized water generated the equivalent 0.5 T and 0.2 T relaxation times respectively.

3.2.1.b - Normal Lung Parenchyma

The lung parenchyma equivalent phantom is more challenging to simulate because of its low PD. In general, this cannot be achieved by using standard phantom materials such as solutions, gels and aqueous media due to the high water content. Our lung parenchyma equivalent requires a low relative PD (~0.3) compared to the tumour. To achieve this, plastic beads (2 mm diameter) that contribute no MR signals are mixed with gelatin (porcine skin gelatin, Sigma Aldrich) in a 70:30 volume ratio. The resulting mixture has the relative PD similar to lung parenchyma. T_1 and T_2 relaxation times are adjusted with the same approach as discussed in the previous section. Our experimental results show that 0.0125 g/L MnCl₂ + gel/plastic bead mixture generates the required 0.5 T relaxation times, and 0.016 g/L MnCl₂ + 0.06 g CuSO₄.5H₂O + gel/plastic mixture generates the required 0.2 T relaxation times.

3.2.1.c - Thoracic Tissues

To simulate the "body noise", the lung compartment is placed in a larger thoracic cage which is filled with substantial amounts of materials that have similar electric conductivity to the body. Approximately 12 litres of salt solution (3.6g/L of NaCl) is used to simulate tissues in the thoracic region. These materials could simulate coil loading similar to that in realistic thoracic imaging condition[7].

3.2.1.d - Absolute PD Adjustment

It must be noted that the aqueous solution (~100% water) is used in this study as a solid tumour equivalent, even though a real tumour, similar to tissue[2], contains only ~75% water[8]. This will result in an overestimation of tumour SNR by 33%. Also, as previously explained, our simulated normal lung parenchyma has been built with the specific *relative* PD to the tumour as indicated in the literature. Therefore, both the tumour region SNR and CNR (i.e. $CNR = \Delta SNR$) are overestimated by 33%. This is compensated by adding additional Gaussian noise to the acquired MR images of the phantom in the post processing steps.

3.2.2 Verification of Contrast Parameters

3.2.2.a - T_1 Measurements

T_1 relaxation times are determined from experiments performed in a 3 T MRI system (Acheiva, Philips Medical System, Cleveland, Ohio) using inversion recovery sequences (TE = 11 ms, TR = 1400 ms) with 6 different inversion times (TI = 100, 200, 300, 400, 500, 600 ms). The 6 acquired images are fed into a T_1 mapping algorithm. One challenge with working with magnitude images is that the signal polarity information is discarded. To address this, the algorithm processes the 6 data points for every pixel in the image by first determining the image with TI closest to the null point (minimum signal) as the “null pixel”. All the data acquired with a TI less than the null pixel are assumed to have negative polarity, while all the data point in the images acquired with a TI greater than the null pixel is assumed to have positive polarity. The null pixel, due to its low SNR and uncertainty in polarity, is discarded, and T_1 is determined as exponential

fitting the remaining 5 data point as described in section 2.3.3. A sample relaxation curve for a sample tumour pixel in the 0.2 T phantom is shown in Figure 3-2.

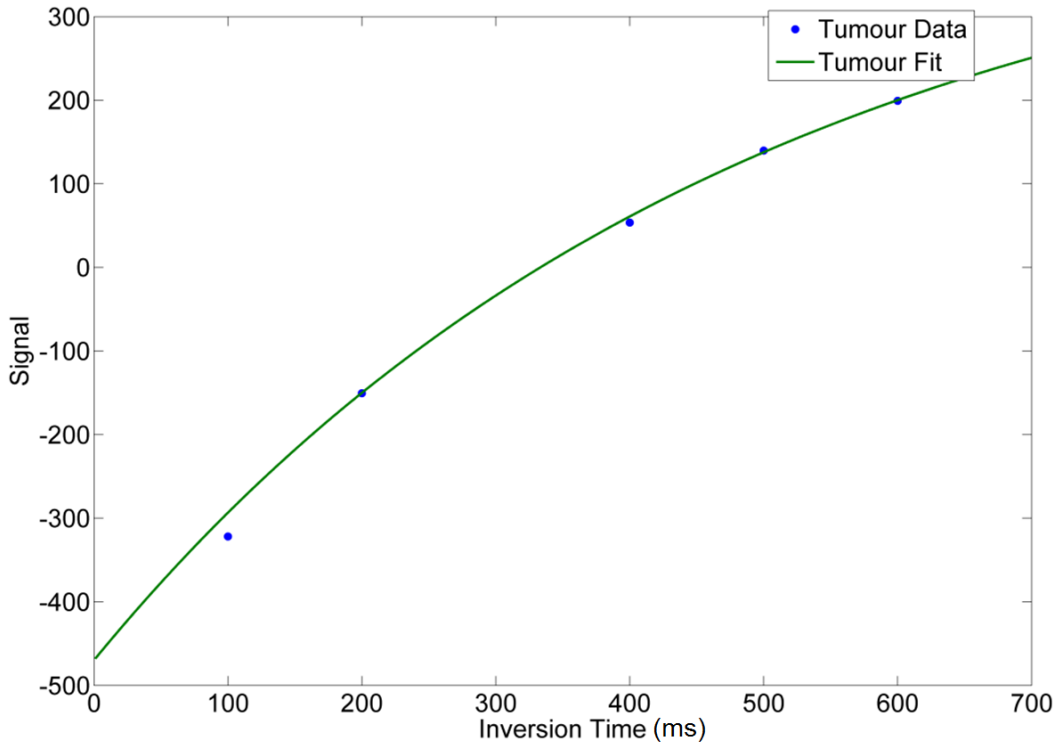


Figure 3-2: T_1 relaxation curve for a representative tumour pixel from the 0.2 T phantom. The data point at 300 ms (the point closest to the null point) is discarded, and the data point at 100 ms and 200 ms are inverted. Signal is expressed in relative units.

3.2.2.b - T_2 Measurements

T_2 relaxation times are measured with a 32 echo multi-spin-echo sequence (TE = 6.2, 12.4, 18.6 ms..., TR = 1048 ms). The data is fitted with a T_2 mapping algorithm. The algorithm creates a 32-point T_2 curve for each individual pixel in the image, and performs an exponential best fit to calculate T_2 . An example of T_2 relaxation curves for the representative pixels in the normal lung tissue and tumour regions of the 0.2 T phantom is shown in Figure 3-3.

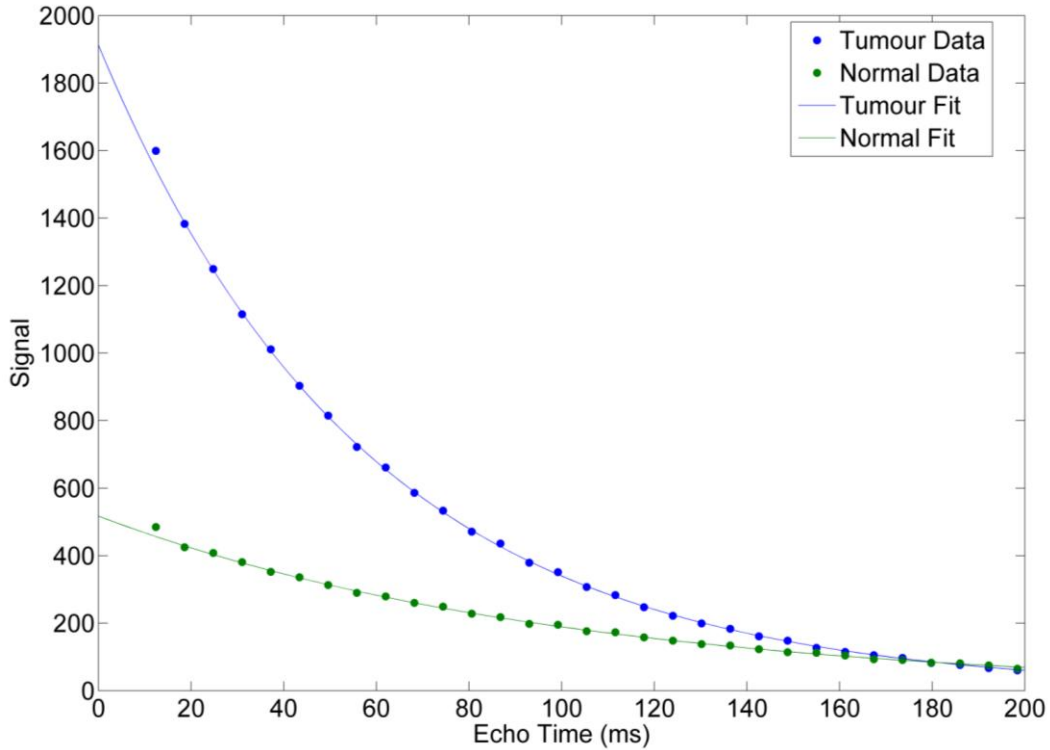


Figure 3-3: 32 echo T_2 relaxation curves for the tumour and normal tissue for the 0.2 T phantom. Signal is expressed in relative units.

3.2.2.c- Relative PD Measurements

Relative PD is measured by generating a PD-weighted spin echo image using short TE and long TR (TE = 11 ms, TR = 2000 ms). Tumour and lung parenchyma region of interests are contoured to determine the mean signals in these regions. Relative PD is calculated as the ratio between the two mean signals.

3.2.3 - Sequence Evaluation

After inserting 0.5 T equivalent phantom in the 3 T scanner, the performance of a fast MRI sequence that will be suitable for real time lung tumour motion tracking in MRI is evaluated. The criterion for successful tracking is set at approximately 4 image frames per second (fps) for the imaging speed. Two sequences were

tested in these experiments. Firstly, a bSSFP sequence (flip angle = 20° , TE = 1.1 ms, TR = 2.2 ms, resolution = 128 x 128, FOV = 400 mm x 400 mm x 20 mm, imaging time = 273 ms). It should be noted that the flip angle of 20° is less than the optimal angle as determined from equation 2.61 in order to satisfy the MR scanner's SAR limitations to maintain imaging speed. Secondly, a FLASH sequence (flip angle = 5° , TE = 1.1 ms, TR = 2.3 ms, resolution = 128 x 128, FOV = 400 mm x 400 mm x 20 mm, imaging time = 293 ms) was also investigated. The flip angle for the FLASH sequence is the optimal angle for tumour signal as calculated from equation 2.58. To ensure sufficient statistical power for comparing the two sequences, 50 samples for each sequence are acquired. The SNR and the CNR of the each acquired image is measured by manually labeling a tumour and lung parenchyma region of interest in the image and recording the mean pixel value as S_{tumour} and $S_{\text{parenchyma}}$ in a defined regions of interest. Noise is measured from a uniform region with no signal in the corner of the real image. The tumour, parenchyma and noise region of interest is applied to all 50 sample images in each sequence to determine the mean and standard deviation values for tumour SNR and CNR. For comparison of the two sequences, no additional noise is added to the image.

3.3 - Results

3.3.1 - Parameter Maps

The T_1 maps for the lung compartment of the 0.2 T and 0.5 T equivalent phantoms are shown in Figure 3-4. For the 0.2 T equivalent phantom, the measured mean and standard deviation of pixel T_1 values within tumour and lung

parenchyma region are 352 ± 4.3 ms and 470 ± 9.3 ms, respectively. For the 0.5 T equivalent phantom, the measured T_1 of the tumour and lung parenchyma are 519 ± 2.4 ms and 604 ± 4.9 ms, respectively.

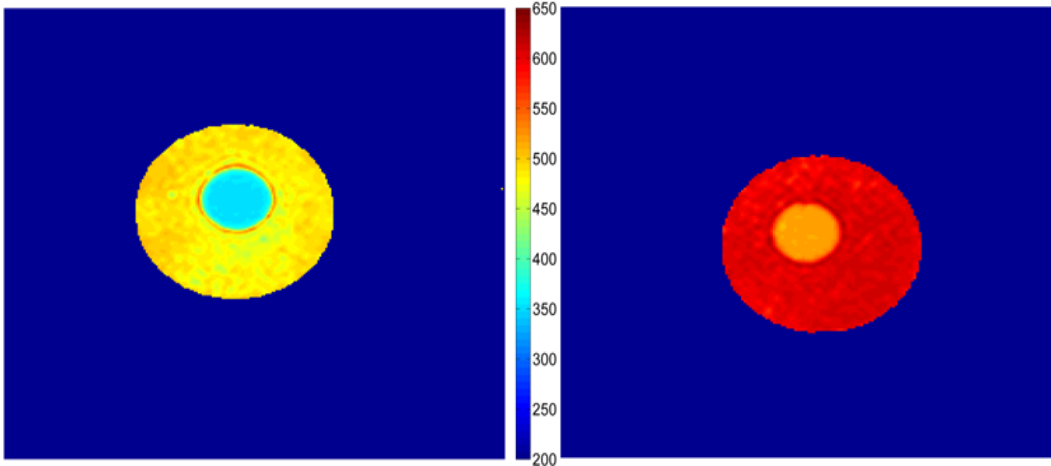


Figure 3-4: T_1 (in ms) parameter map of the lung compartment of the 0.2 T (left) and the 0.5 T (right) equivalent phantom.

The T_2 maps for the lung compartment in 0.2 T and 0.5 T equivalent phantoms are shown in Figure 3-5. For the 0.2 T equivalent phantom, the measured mean and standard deviation of pixel T_2 values for tumour and lung parenchyma are 67 ± 1.5 ms and 83 ± 5.2 ms, respectively. For the 0.5 T equivalent phantom, the measured T_2 for tumour and lung parenchyma are 61 ± 1.9 ms and 97 ± 5.9 ms, respectively.

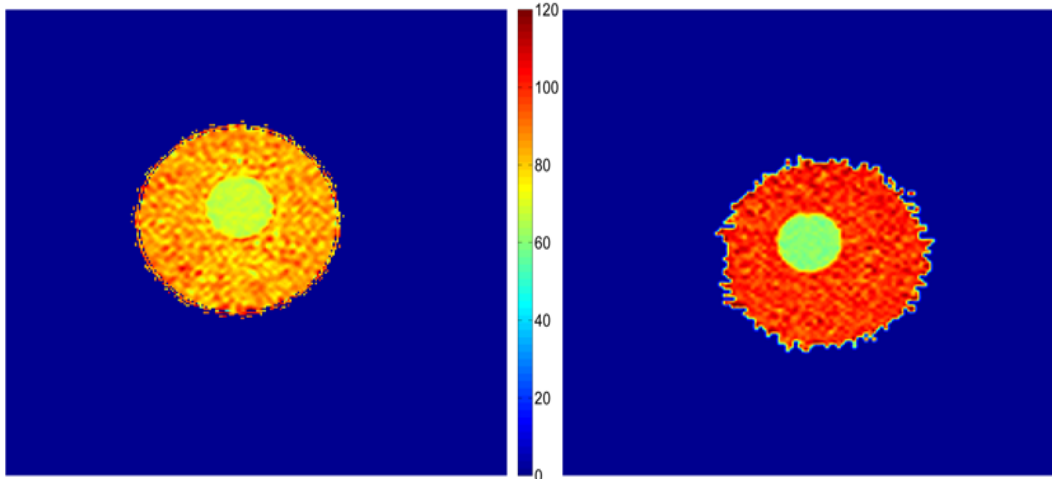


Figure 3-5: T_2 (in ms) parameter map of the lung compartment of the 0.2 T (left) and the 0.5 T (right) equivalent phantoms.

The proton density maps are shown in Figure 3-6. Relative parenchyma-to-tumour PDs for the 0.2 T and 0.5 T phantoms are 0.3 and 0.27, respectively.

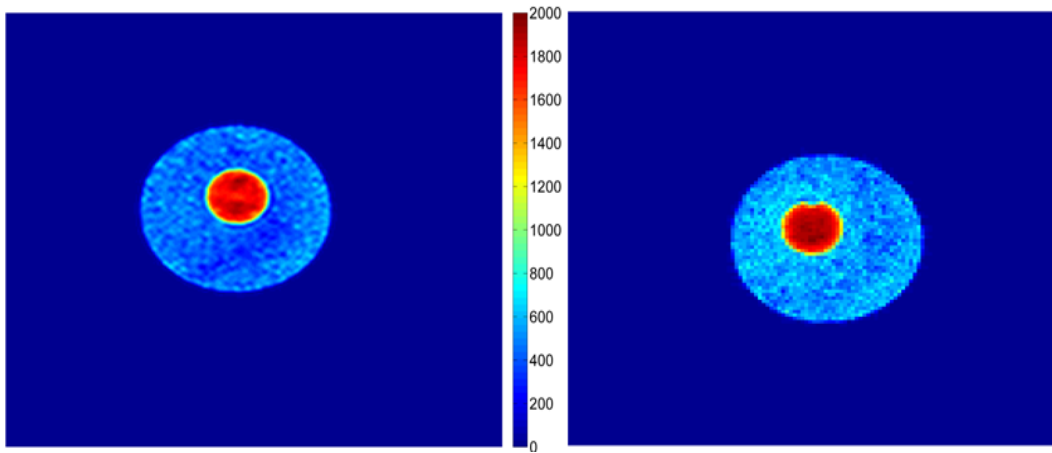


Figure 3-6: PD maps for lung compartment of the 0.2 T (left) and 0.5 T (right) equivalent phantoms.

These parameters are compared against literature values in Tables 3.1 and 3.2.

Table 3.1 MR contrast parameters of the 0.2 T equivalent lung phantom compared against literature values. Measured contrast parameters are expressed as mean±SD of pixel values within a region of interest.

	Lung Tumour		Normal Lung Parenchyma	
	Literature	Measured	Literature	Measured
T_1 Mean±SD (ms)	372±185[3]	352±4.3	455±86[3]	470±9.3
T_2 Mean±SD (ms)	69±45[3]	67±1.5	79±29[3]	83±5.2
Relative PD to tumour	N/A	N/A	0.19 - 0.34[1,2]	0.27

Table 3.2 MR contrast parameters of the 0.5 T equivalent lung phantom compared against literature values. Measured contrast parameters are expressed as mean±SD of pixel values within a region of interest.

	Lung Tumour		Normal Lung Parenchyma	
	Literature	Measured	Literature	Measured
T_1 Mean±SD (ms)	532±271[3]	519±2.4	599±114[3]	604±4.9
T_2 Mean±SD (ms)	69±45[3]	61±1.9	79±29[3]	97±5.9
Relative PD to tumour	N/A	N/A	0.19 - 0.34[1,2]	0.30

3.3.2 - Sequence Evaluation

The 50 bSSFP images have an SNR (mean ± std) of 130 ± 8.0 and a CNR (mean ± std) of 87 ± 5.2 whereas the 50 sample FLASH sequence generated a tumour SNR of 45 ± 2.4 and a CNR of 32 ± 1.7 . Two sample t-test shows that both CNR ($p < 0.00001$) and SNR ($p < 0.00001$) for the bSSFP images are higher compared

to FLASH. While some banding artefacts can be observed on the bSSFP acquired images but they are not located in the central tumour region of the image.

3.4 Discussion

We have constructed a phantom that can be used to mimic the contrast parameters of lung tumour and lung tissue at magnetic fields of 0.2 T and 0.5 T in the images that are actually obtained in a clinical 3 T MRI system.

The MR contrast parameters (PD, T_1 and T_2) of the 0.2 T and 0.5 T equivalent phantoms, measured at the 3 T scanner, are shown to match well with the reported low field values in the literature. The phantoms are therefore expected to mimic the CNR of images acquired at a lower field after the required amounts of noise is added for sequences that produce images with PD, T_1 and T_2 weighting. It should be noted that we did not attempt to match T_2^* of the phantom to literature values due to the difficulty in controlling T_2^* . This phantom is therefore somewhat less accurate in predicting CNR in low field images of a T_2^* weighted sequence (i.e. FLASH) in the acquired images in 3 T MRI. However, bSSFP is likely to generate higher CNR in images as compared to FLASH as explained below.

Recall that for the phantoms, the CNR for the lung tumour is $CNR = SNR_{Tumour} - SNR_{Parenchyma}$. In our phantom, the plastic bead/gelatin interfaces may not fully simulate the air-tissue interface of the lung parenchyma in low fields, resulting in an incorrect T_2^* , which may lead to some error in the predicted $SNR_{Parenchyma}$ for the T_2^* weighted FLASH sequence. Let's assume that the measured $SNR_{Parenchyma}$ for the FLASH image is not correct, leading to an underestimation of CNR for the FLASH sequence, and consider the scenario of greatest CNR underestimation, in

the case where $\text{SNR}_{\text{parenchyma}}$ is actually zero ($\text{CNR} = \text{SNR}_{\text{Tumour}}$). Even in this case, the $\text{SNR}_{\text{Tumour}}$ of the FLASH sequence (45 ± 2.4) remains significantly lower ($p < 0.00001$) compared to the CNR of the bSSFP sequence of 87 ± 5.2 . The banding artefacts in the bSSFP images appear in the peripheral regions in the 3 T images and do not significantly affect the visibility of tumour in the phantom. With the higher CNR as well as the imaging speed, bSSFP is chosen as the sequence for the tumour tracking study described in the next chapter.

3.4 - References

1. Hatabu H, Alsop AC, Listerud J et al., T2* and proton density measurement of normal human lung parenchyma using sub millisecond echo time gradient echo magnetic resonance imaging. *European Journal of Radiology* 29:245, 1999
2. Schmidt HC, Tscholakoff D, Hricak D, and Higgins CB, MR Image-Contrast and Relaxation-Times of Solid Tumours in the Chest, Abdomen, and Pelvis. *Journal of Computer Assisted Tomography* 9:738, 1985
3. Bottemley PA, Hardy CJ, Argersinger RE and Allenmoore G, A Review of H-1 Nuclear-Magnetic-Resonance Relaxation in Pathology - Are T1 and T2 Diagnostic? *Med. Phys.* 14:1, 1987
4. Bergin CJ, Glover GH, and Pauly JM, Lung Parenchyma - Magnetic-Susceptibility in MR Imaging. *Radiology* 180:845, 1991
5. Boss A, Schaefer S, Martirosian P et al., Magnetic resonance imaging of lung tissue: Influence of body positioning, breathing and oxygen inhalation on signal decay using multi-echo gradient-echo sequences. *Investigative Radiology* 43:433, 2008
6. Kato H, Kuroda M, Yoshimura et al., Composition of MRI phantom equivalent to human tissues. *Med. Phys.* 32:3199, 2005
7. Och JG, Clarke GD, Sobol WT et al., Acceptance Testing of Magnetic-Resonance-Imaging Systems - Report of Aapm Nuclear-Magnetic-Resonance Task Group No-6. *Med. Phys.* 19:217, 1992
8. Fleer CTG, Carpenter RG, and Florence I, Variability in the water, sodium, potassium, and chloride content of human skeletal muscle. *Journal of Clinical Pathology* 18:74, 1965.

Chapter 4 - Real Time Tumour Tracking Study

4.1 - Overview

The previous chapter described the design and fabrication of phantoms that could mimic the MRI contrast parameters of the lung tumour and lung tissue in the images obtained with a clinical 3 T MRI system. In this chapter, the use of these two phantoms is described in imaging experiments that are specifically suited to demonstrate the real time motion tracking of lung tumours. We aim to test the feasibility of a real time tumour tracking system on phantom images that would best reflect the image quality of lung tumour MR images at low fields (i.e. 0.2 T and 0.5 T) especially in terms of contrast to noise ratio (CNR). The lung contrast phantoms are subjected to realistic motion patterns by a programmable motor while being imaged with a real time dynamic MRI sequence. The images are post-processed to reflect low field CNR, and an automatic contouring algorithm is applied to them. The contours are evaluated for their accuracy against some reference contours known *a priori* or determined using slow, high resolution MRI sequences.

4.2 - Materials and Methods

4.2.1 - Phantom Experiment Setup

Our phantom and its experimental setup are shown in Figure 4-1. The phantom is placed the MRI's field of view, and it contains a moving "lung compartment" that can freely slide within the "thorax" region. In the lung compartment, the lung "tumour model" (red circle) is located approximately at the center of the lung

compartment, and the tumour model is surrounded by simulated lung tissue (green rectangle). The lung compartment is attached to a programmable motor via a rigid aluminum rod, creating 1-D motion parallel to the aluminum rod. This motion is in the same direction as the patient's superior-inferior (SI) direction that is known to contain the largest motion of the lung tumour caused by free-breathing. The aluminum rod is grounded to the wave guide using a small amount of copper tape to eliminate any noise induced by the metal rod. To provide an independent, reference measurement of the lung tumour position, an optical encoder (model #: AEDR-8300-1Q2, Avago technologies, San Jose, CA) was attached to the thoracic cage as shown in Figure 4-1. Paired with the encoder, a reflective code strip (resolution: 180 lines per inch) is attached to the moving compartment that contains the tumour model. Because all other parts of the phantom are stationary, and the tumour model is fixed in the lung compartment, any change in the tumour position in SI direction is measured by the encoder as a change in counts (1 count \approx 0.035 mm).

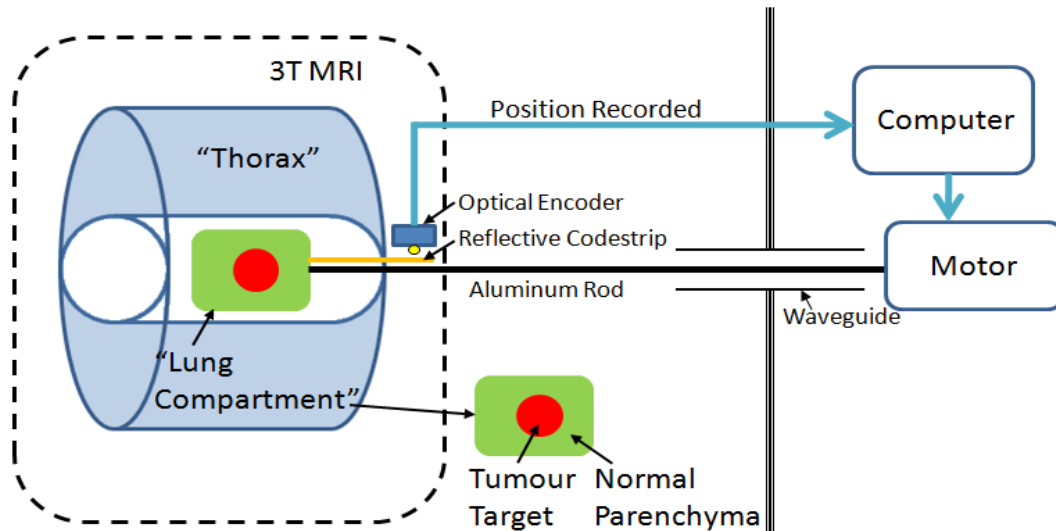


Figure 4-1 Schematic diagram of the experiment set up

4.2.2 - Tumour Shapes and Motion Patterns

A series of dynamic studies were performed with the phantom to evaluate the performance of our auto-contouring algorithm in the equivalent low field MR images. For both the 0.2 T and 0.5 T equivalent contrast parameters, we created two separate lung compartments differing in tumour shape: a spherical tumour model, and another with an elongated, irregularly shaped tumour model. Hence, the study was performed with four different lung compartments in total. In each case, the lung compartment was moving inside of the thoracic cage during the MRI data acquisition.

The lung compartment was driven in accordance with four different pre-determined motion patterns during the dynamic study. The motion patterns used in our dynamic studies are shown in Figure 4-2. The first pattern is a sine wave of 40 mm peak-to-peak amplitude and a period of 4 seconds. This pattern was created to simulate very large amount of regular, predictable lung tumour motion.

The other three patterns were obtained from three different patient datasets. Suh *et al* [1] analyzed thoracic and abdominal tumour motions from 42 patients by using a Cyberknife Synchrony system (Accuray Incorporated, Sunnyvale, CA) incorporating implanted fiducials in the patient imaged by a stereo system of X-ray projection imaging. This group provided us with their clinical data containing 3D lung tumour positions that were estimated and recorded with a temporal frequency of 25 Hz during the actual treatment. Because lung tumours show the largest motions in the superior-inferior (SI) direction, we selected three lung tumour motion patterns that showed relatively large SI motions, approximately 15 mm amplitude on average and with varying periods. Each study took approximately 3 minutes, and the patterns of Figure 4-2 represent 1D motion of lung tumour in SI direction.

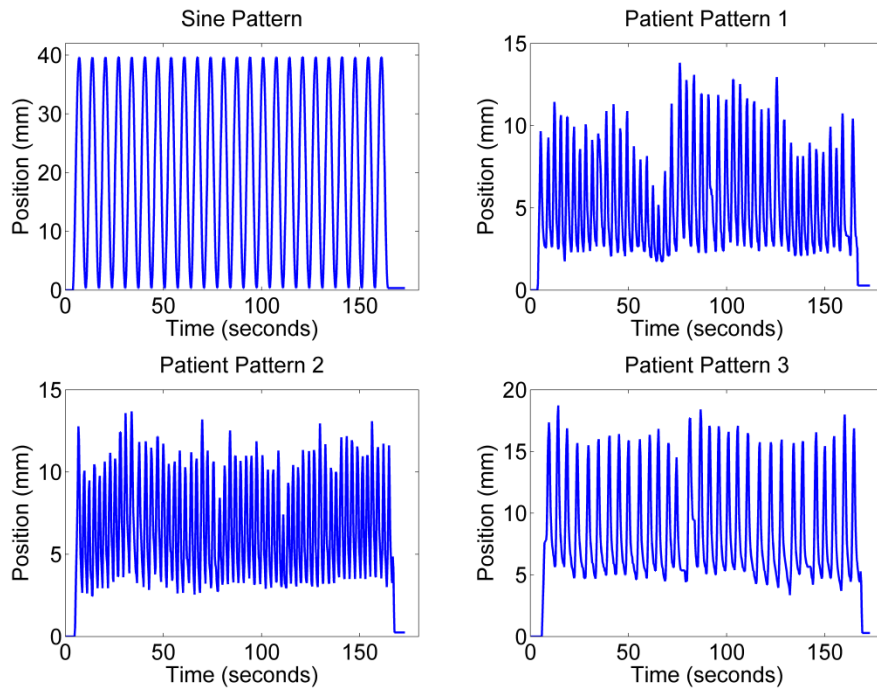


Figure 4-2: Motion Patterns used to drive lung compartment. A sine pattern (upper left) and three lung tumour motion patterns from patient data

4.2.3 - MR Imaging Sequences

For each motion pattern, as well as a static pattern, we performed the following two MR image acquisitions in order: (1) a high resolution turbo-spin-echo (TSE) scan acquired when the tumour is stationary in its starting position, followed by (2) dynamic bSSFP scans while the tumour is undergoing the prescribed motion pattern.

TSE scan (FOV = 400 mm x 400 mm, voxel size = 0.4 mm x 0.4 mm x 4 mm, 5 slices, TE = 87 ms, TR = 1798 ms) was chosen as a reference image due to its high SNR, very high resolution and minimal susceptibility to artefacts. Due to its high resolution, the images were sharp enough to visualize the thin walls (~0.3

mm) of the tumour model, allowing the true shape of the tumour to be manually contoured. The middle slice that covers the largest extent of the tumour is contoured manually and considered as a reference shape in this study. The tumour shapes obtained with the other dynamic MR image acquisition were compared to this reference shape in each tumour model.

For dynamic imaging, we used a 2D bSSFP sequence acquiring images at approximately 4 fps (identical FOV to TSE scan: 400 mm x 400 mm, voxel size = 3.1 mm x 3.1 mm x 20 mm, TE = 1.1 ms, TR = 2.2 ms, dynamic scan time = 275 ms) in the horizontal plane through the middle of the tumour model, known as the coronal plane. Prior to each dynamic image acquisition, an external synchronization pulse at known time point is sent to the optical encoder. Using this pulse, the optical encoder records the position of the tumour at the mid-point of each dynamic data acquisition when the signal acquisition is occurring at the center of k-space. The first images of the dynamic scans are acquired prior to the commencement of motion, with the phantom in the same position as the reference TSE scan. These images are visually inspected to ensure alignment with the high-resolution TSE image.

All MR images were acquired with a 6 channel Philips torso coil. Noise is measured as the standard deviation for each individual image in a 10x10 pixel region in the corner of the image containing no MR signal. To ensure there is no positive noise bias, the noise is measured in the real and imaginary images reconstructed by the scanner and averaged, rather than measured in the magnitude images

4.2.4 - Image Post Processing

Gaussian noise is added to the images that were acquired on the 3 T MRI system, in order to reflect the lower CNR at 0.5 T and 0.2 T. Downscaling of CNR from 3 T images could be achieved by linear CNR scaling, amplifying the measured background noise by a factor of 6 and 15 for 0.5 T and 0.2 T images to reduce CNR according to equation 2.65. As mentioned in section 3.2.1.4, noise is increased by another 33% to account for the difference in absolute PD between the real solid tumour and the aqueous tumour model that was used in our phantom. Combining these two corrections, noise amplification factors of 8 and 20 were applied to simulate the 0.5 T and 0.2 T images, respectively. Noise amplification is achieved by the addition of Gaussian noise to the images. Assuming statistical independence, the required standard deviation of the added noise is derived from the standard deviation of measured noise using the equations

$$(N \cdot \sigma_{meas})^2 = \sigma_{meas}^2 + \sigma_{added}^2 \quad (4.1)$$

$$\sigma_{added} = \sqrt{N^2 - 1} \cdot \sigma_{meas} \quad (4.2)$$

where N is the noise amplification factor, σ_{meas} and σ_{added} are the standard deviations of the measured and added noise, respectively. Noise is independently measured and amplified in the real and imaginary images and combined to generate the required noise degradation in the magnitude images. After the noise addition, the image is interpolated to a 256 x 256 matrix prior to auto-contouring. The auto-contouring algorithm is developed and described by Yun *et al*[2] and it

will be only briefly discussed here. This algorithm requires the user to pick a sample dynamic image and contour the tumour and a larger "background" region covering the likely extent of the moving tumour. For each test dynamic image, the tracking algorithm determines a rather large but the most likely region of the tumour centered at the point of maximum correlation between the test images and the *a priori* known background region. To the most likely containing the tumour region, the algorithm applies a series of edge determining algorithm(s) to determine the shape of the tumour, allowing for adaptation of small changes in tumour shape. The auto-contoured shape is saved for further analysis.

4.2.5 - CNR Measurements

While a single image is sufficient to measure CNR, more measurements would ensure stronger statistical power. To measure CNR, at the end of each dynamic scan (~3 minutes), an extra set of 100 images are acquired when the phantom is stationary, located at the last position of the motion pattern. As a result, 20 different sets of images (2 tumour models x 2 field strengths x (4+1) motion/static patterns = 20 sets) were obtained, each set containing 100 images. Using these images, the CNR is measured for each set. As the phantom is stationary, a manually determined region of interest within the tumour and the normal tissue parenchyma is applied to all 100 images in the set. The mean pixel values of these regions of interest were used to calculate the signal difference in Equation 2.64. Noise is measured as the standard deviation of pixels in a 10x10 region in the corner of the real and imaginary images. This noise measurement is performed

after required noise has been added for CNR degradation at lower magnetic field, but prior to the 256x256 interpolation.

4.2.6 - Data Analysis

For each dynamic study (~600 images), the post-processed images are fed into the auto-contouring algorithm offline. The algorithm returns an auto-contoured tumour shape and its centroid from each image, and these results were used to evaluate the auto-contouring and tracking performance of our algorithm.

4.2.7 - Contour Shape Fidelity

To evaluate the quality of the contours generated from the auto-contouring algorithm, we first manually contoured the tumour in a reference TSE scan (Figure 4-3). From this manual contour, a binary mask was generated, and this was considered as a standard tumour shape. The optical encoder readings were used to linearly translate this mask, generating a standard set of masks that corresponds to the standard tumour shape for the time-point of each dynamic image. Similarly, a set of auto-contoured masks is produced from the auto-contouring algorithm for each dynamic image.

The auto-contoured mask in the dynamic images has lower resolution (256x256) than the manually contoured mask (1024x1024). For comparison, the low resolution mask is re-sampled to 1024x1024 resolution using the nearest neighbour method, which maintains the pixilated appearance of the low resolution image. We performed a one-to-one comparison of the tumour shape between the

reference mask and the mask from each dynamic image, and their similarities are evaluated by calculating Dice's coefficient defined as follows.

$$DC = \frac{Area(ROI_{std} \cap ROI_{auto})}{\{Area(ROI_{std}) + Area(ROI_{auto})\}/2} \quad (4.3)$$

Perfect agreement between the two contours would give a dice coefficient of one.

A mean DC is calculated for each set of images.

4.2.8 - Centroid Position Accuracy

We also evaluated the algorithm's ability to accurately determine and track the centroid position of a moving tumour. Firstly, we determined an initial centroid position of the tumour from a high resolution image. This image was acquired when the tumour was located on its initial position of the motion pattern, and the tumour shape was manually contoured. The initial centroid position served as the reference point (i.e. zero count) for optical encoder reading. Secondly, the tumour position change during each dynamic acquisition was continuously recorded by the encoder. As previously explained, the encoder reads the tumour position when the signal acquisition is occurring at the center of k-space. Thirdly, the centroid position of the tumour in each dynamic image was determined by the auto-contouring algorithm. Lastly, we made one-to-one comparison of the centroid position of the tumour in each image, between the encoder reading and the result from the auto-contouring algorithm applied to the dynamic images.

Mean and standard deviation of the difference between the two are calculated from all the images within the motion pattern. Root mean square error (RMSE) is also calculated to give an indication of overall error as follows.

$$RMSE = \sqrt{\frac{\sum_{i=1}^n (y_{i,centroid} - y_{i,contour})^2}{n}} \quad (4.4)$$

Where $y_{i,centroid}$ is the centroid position of the auto-contoured tumour and $y_{i,encoder}$ is the position of the tumour measured by the optical encoding device.

4.3 - Results

4.3.1 - Simulated Lung Tumour Images with Low Field CNR

A close up view of the tumour and its surrounding tissue acquired using TSE and post-processed bSSFP is shown in Figure 4-3. As predicted, the thin wall of tumour container is visualized by the high resolution TSE scan to aid in manual contouring, but it is not detected in the bSSFP image and should have no impact on the auto-contouring algorithm.

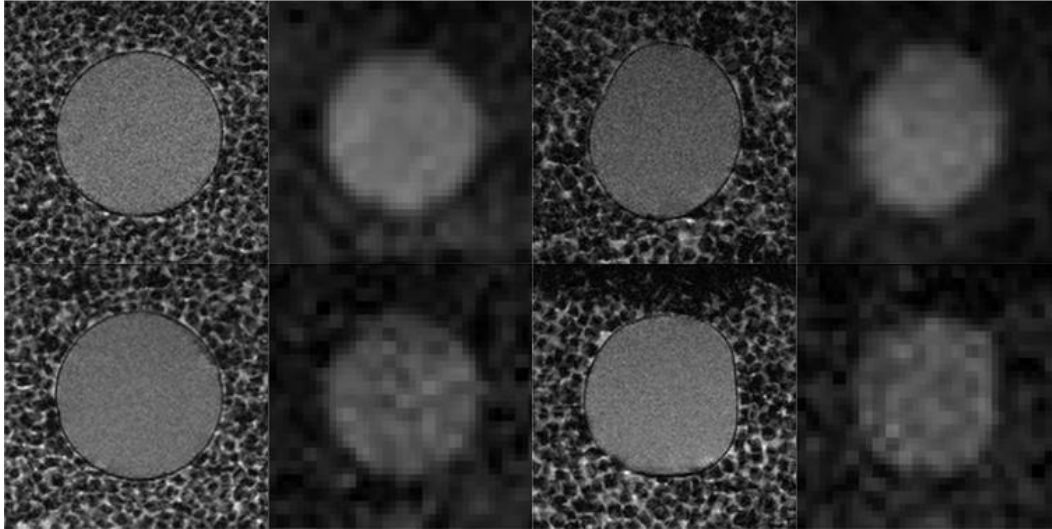


Figure 4-3 First row, from left to right: 1) High Resolution TSE (middle slice) image. 2) Noise added (0.5 T) dynamic bSSFP scan. 3) High Resolution TSE (middle slice) image for a non spherical tumour. 4) Corresponding noise added (0.5 T) dynamic bSSFP scan. Second row: equivalent images for 0.2 T experiments

3.3.2 - CNR of Acquired Images

After the images are acquired using the 3 T scanner, noise is added to generate the 0.2 T and 0.5 T equivalent images (Figure 4-4). The CNR of these images are shown in Table 4.1. The measured CNR ranges from 10.3 - 12.3 in 0.5 T equivalent images and from 4.2-4.5 in 0.2 T equivalent images. The mean and standard deviation of the CNR is 11.5 ± 1.2 and 4.3 ± 0.4 in the equivalent 0.5 T and 0.2 T images.

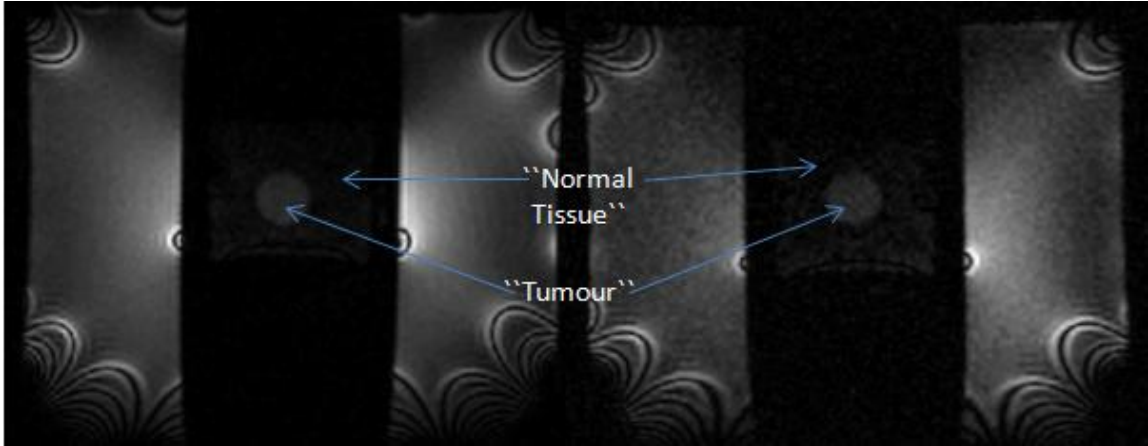


Figure 4-4: Sample dynamic bSSFP images from the experiment, after noise addition. Image on the left reflects 0.5 T equivalent CNR whereas image on the right reflects 0.2 T equivalent CNR.

Table 4.1: CNR for spherical and non-spherical tumour models in 0.5 T and 0.2 T equivalent images. The standard deviation of the CNR is given in brackets.

	0.5 T CNR		0.2 T CNR	
	Spherical Tumour	Non-Spherical Tumour	Spherical Tumour	Non-Spherical Tumour
No Motion	12.3 (0.9)	10.3 (0.8)	4.3 (0.4)	4.5 (0.4)
Sine Pattern	12.3 (1.0)	10.5 (0.9)	4.4 (0.3)	4.4 (0.4)
Patient Pattern 1	12.1 (1.0)	10.7 (0.8)	4.4 (0.4)	4.3 (0.3)
Patient Pattern 2	12.1 (1.0)	11.2 (0.8)	4.4 (0.4)	4.3 (0.3)
Patient Pattern 3	11.9 (0.9)	11.2 (0.9)	4.2 (0.4)	4.2 (0.4)

4.3.3 - Contour Shape Fidelity

The Dice's coefficient values from our phantom experiment are evaluated and shown in Table 4.2. A mean Dice's coefficient of > 0.96 is achieved in the 0.5 T equivalent images and a mean Dice's coefficient of > 0.93 is achieved in the 0.2 T equivalent images.

4.3.4 - Centroid Position Accuracy

The difference between the centroid positions determined by auto-contouring and those from the encoder reading are summarized in Table 4.2. Mean and standard deviation represents the systematic and random errors in tumour tracking, while root mean square error (RMSE) is a representation of overall error. RMSE of < 0.55 mm is achieved for 0.5 T equivalent images, whereas a RMSE of < 0.92 mm is achieved for 0.2 T equivalent images.

Table 4.2: Dice's Coefficient, centroid error and RMSE in auto-contouring and tracking

	Dice's Coefficient Mean(Std)	Centroid Error (mm) Mean(Std)	Centroid RMSE (mm)
0.5 T CNR (sphere)			
No Motion	0.965 (0.009)	-0.05 (0.41)	0.41
Sine Pattern	0.962 (0.009)	0.06 (0.46)	0.47
Patient Pattern 1	0.966 (0.007)	0.08 (0.41)	0.42
Patient Pattern 2	0.963 (0.009)	-0.20 (0.46)	0.50
Patient Pattern 3	0.961 (0.006)	0.29 (0.46)	0.55
0.5 T CNR (non-sphere)			
No Motion	0.960 (0.005)	0.17 (0.31)	0.35
Sine Pattern	0.963 (0.006)	0.01 (0.35)	0.35
Patient Pattern 1	0.966 (0.005)	0.19 (0.36)	0.41
Patient Pattern 2	0.966 (0.005)	0.07 (0.37)	0.38
Patient Pattern 3	0.967 (0.004)	0.08 (0.37)	0.38

0.2 T CNR (sphere)

No Motion	0.953 (0.010)	0.26 (0.69)	0.74
Sine Pattern	0.950 (0.011)	0.10 (0.74)	0.75
Patient Pattern 1	0.953 (0.010)	0.21 (0.70)	0.73
Patient Pattern 2	0.951 (0.011)	-0.11 (0.70)	0.70
Patient Pattern 3	0.948 (0.013)	0.23 (0.70)	0.73

0.2 T CNR (non-sphere)

No Motion	0.947 (0.015)	-0.06 (0.65)	0.66
Sine Pattern	0.940 (0.018)	0.10 (0.88)	0.90
Patient Pattern 1	0.936 (0.019)	0.14 (0.88)	0.90
Patient Pattern 2	0.939 (0.019)	0.22 (0.90)	0.92
Patient Pattern 3	0.935 (0.021)	0.23 (0.89)	0.92

4.4 - Discussion

The fidelity of auto-contoured tumour shape was evaluated by calculating mean Dice's coefficient, which were > 0.96 and > 0.93 in the 0.5 T and 0.2 T equivalent images, respectively. Centroid tracking accuracy using our algorithm was measured in terms of RMSE values, which were < 0.55 mm and < 0.92 mm for the 0.5 T and 0.2 T equivalent images, respectively. As expected, tumour tracking accuracy is improved by the higher CNR provided at 0.5 T. The results suggests that our auto-contouring algorithm is successful in contouring the lung tumour model in both 0.2 T and 0.5 T equivalent images. Also, 0.2 T and 0.5 T MR systems can provide the necessary CNR at the temporal resolution (~ 4 fps) required for tracking lung tumour motion.

An advantage in performing this type of phantom study is that it allows for a "gold-standard" measurement for both tumour shape and position, and therefore the auto-contouring and tracking performance can be quantified. This would not be possible in a patient study mainly due to inter- and intra-observer variability in contouring. From the phantom study, we demonstrated a promising application of low field linac-MR systems in lung tumour tracking. However, there are several issues that would need to be addressed in future studies.

Our phantom is limited to 1-D motion in the SI direction, while tumours in patient often have a 3D motion trajectory. In current linac based treatments, as well as in future linac-MR based treatments using our laboratory's designs, radiation beams rotate around the SI axis of the patient. Hence, if the intra-fractional MR imaging is performed from the beam's eye view, the 2D imaging presented here may be sufficient for tumour tracking in SI and one more direction in that imaging plane. In this scenario, our algorithm can be used to detect in-plane changes in tumour position and adjust the multi-leaf collimator accordingly. However, a potential problem that can arise is through-plane motion (motion orthogonal to the imaging plane) of the tumour. Tumours can potentially move out of the imaging plane. Although numerous studies have demonstrated that the largest lung tumour motion occurs in SI direction[3], smaller motions in anterior-posterior and left-right directions could contribute to the out of imaging plane motion.

Potential solutions to this problem include adjusting the slice thickness of the imaging plane to ensure the tumour remains in the imaging plane. Also, our CNR measurements suggest that at 0.5 T, there is potentially enough CNR (10.3 - 12.3)

to allow image accelerations via various techniques such as parallel imaging. This opens up the possibility to perform intra-fractional multi-slice or 3D imaging, which will be investigated in future studies. However, one must also be cautious in these approaches, as there is a CNR penalty that affects accuracy in tumour tracking, as shown by the greater centroid error and lower mean Dice's coefficients for the 0.2 T equivalent images.

Several factors can actually lead to an improvement of image quality when imaging is performed in a low field MRI. Firstly, in our experiments, the flip angle is limited by specific absorption rate (SAR) safety limits due to the very short TR required for fast imaging. SAR is proportional to the square of the main magnetic field[4], so the lower SAR at low fields will allow greater freedom in choosing the flip angle. This could enhance the CNR available to the bSSFP images[5]. Secondly, banding artefacts, while not affecting the central area of the tumour in our scans, are clearly visible in the periphery of the image in 3 T. These banding artefacts will be considerably less severe in a low field MRI due to the improved local field homogeneity[6].

The algorithm's auto-contouring ability is demonstrated in low field dynamic MR imaging situations with solid, moving tumours in a phantom setting (Dice's coefficient > 0.96 and > 0.93 in 0.5 T and 0.2 T equivalent images). Some issues such as 3D motion, as well as the presence of other high contrast structures (such as blood vessel) are present in patient images but not accounted for in the phantom. The next chapter describes some initial work performed with a patient with lung cancer.

4.5 - References

1. Suh Y, Dieterich S, Cho B, and Keall PJ, An analysis of thoracic and abdominal tumour motion for stereotactic body radiotherapy patients. *Phys. Med. Biol.* 53, 3623, 2008.
2. Yun J, Mackenzie M, Robinson D et al., Real-Time MR Tumour Tracking Using a Linac-MR system. *Med. Phys.*, 37: 3153, 2010.
3. Keall, PJ, Mageras GS, Balter JM et al., The management of respiratory motion in radiation oncology report of AAPM Task Group 76. *Medical Physics*, 33(10):3874, 2006.
4. Bernstein MA, King KF, Zhou XJ, *Handbook of MRI pulse sequences*, Academic Press, 2004.
5. Scheffler K and Lehnhardt S, Principles and applications of balanced SSFP techniques. *European Radiology* 13: 2409, 2003
6. Wieben O, Francois C, and Reeder SB, Cardiac MRI of ischemic heart disease at 3 T: Potential and challenges. *European Journal of Radiology* 65:15, 2008.

Chapter 5 Initial Experience in-vivo Patient Tumour

5.1 - Overview

This chapter describes the preliminary work of applying the bSSFP sequence to track mobile lung tumour in *vivo*. Imaging is performed in a clinical 3 T MRI; however, the image CNR is degraded to match the equivalent CNR in low field MRI. This experiment serves two purposes. The first purpose is to compare the CNR measured in the patient with the CNR measured in the phantom. In Chapter 2, it was argued that one cannot accurately predict CNR of low field images by simple linear scaling of CNR from images acquired at 3 T, as secondary effects such as T_1 compensates for the signal losses from lower field. However, compared to the impact of lowering the main magnetic field, these effects are of secondary importance. We therefore expect the CNR estimated from linearly scaled 3 T patient images to be within a similar order of magnitude of the CNR estimated in the phantom experiments. The second purpose of this preliminary study is to generate useful *in-vivo* images to verify the feasibility of the auto-contouring system *in-vivo*. *In-vivo* images are degraded to have equivalent low field CNR predicted from our phantom study, in order to evaluate the performance of the auto-contouring software using these equivalent images.

5.2 - Methods and Materials

As this is preliminary work, a single patient with a tumour in the right posterior region of the lung is studied in this chapter. A 3D anatomical scan is performed,

and a reconstructed transverse plane visualizing the tumour is shown in Figure 5-1, in which the solid lung tumour is clearly visible.

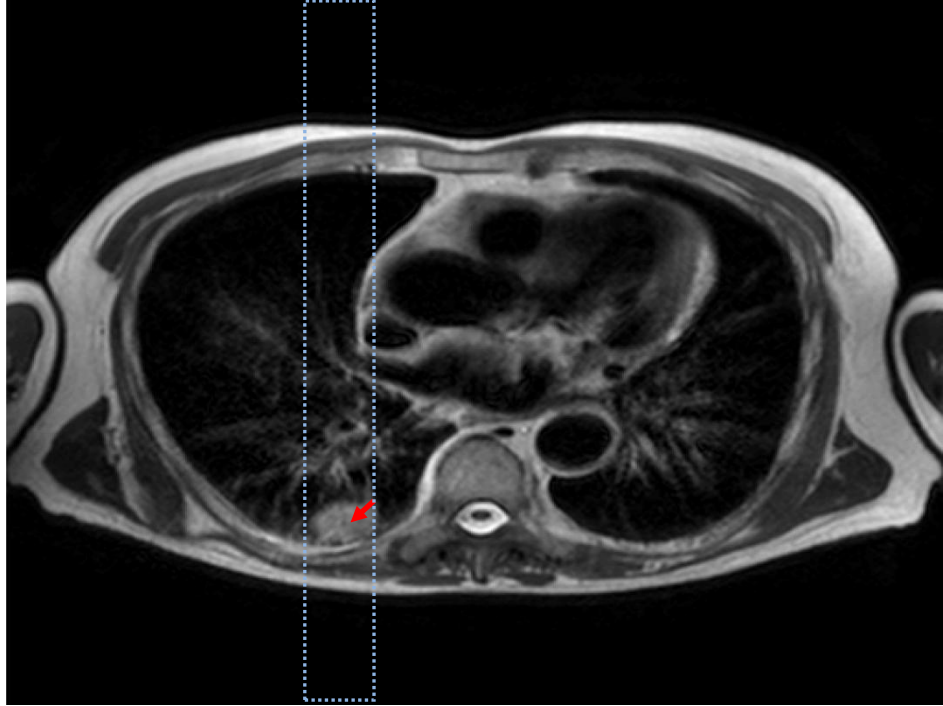


Figure 5-1: A transverse view of the patient. The solid tumour is indicated by the red arrow. The blue dotted lines encompass the thick sagittal imaging plane used in cine imaging.

5.2.1 - Dynamic MR Imaging Sequence

For this patient, a bSSFP sequence, similar to that used in phantom studies, is used: 2D bSSFP sequence acquired at approximately 4 fps, a FOV of 400 mm x 400 mm, voxel size = 3.1mm x 3.1mm x 20 mm, TE = 1.1 ms, TR = 2.2 ms, and Dynamic Scan Time = 273 ms. A sagittal plane is chosen for our dynamic sequence because that plane encapsulates structures close to the tumour that pose the greatest challenge to the tumour auto-segmentation algorithm.

5.2.2 - CNR Measurement and Comparison to Phantom Results

Tumour CNR is measured directly on the 3 T images in the sagittal plane. This is performed by manually contouring a region of interest in the lung tumour and background parenchyma in 15 images ($0.275\text{s} * 15 = 4.1\text{s}$, approximately 1 breathing cycle) to calculate CNR. Unlike the phantom, the patient's CNR measurements must be measured in the presence of motion, requiring ROI's to be manually contoured on each individual image. The CNR is therefore measured with a smaller sample size of 15. Linear CNR scaling factor of 6 and 15 is then applied, using the approach discussed in section 4.2.5, to estimate the equivalent CNR at 0.5 T and 0.2 T. These values are then compared with the CNR predicted by the phantom.

5.2.3 - CNR Modification of Images for Tumour Tracking

In order to test the tracking algorithm in a realistic *in-vivo* setting, the noise was amplified to match the CNR predicted by the phantom, which included relaxation effects, rather than by a factor strictly determined by linear scaling due to the change in the main magnetic field. Noise is added to the 3 T images to reflect those measured using the phantom as in equations 4.1 and 4.2. However, in this instance, the noise amplification factor would be the ratio between the measured CNR in the 3 T patient image and the desired 0.5 T/0.2 T CNR measured from the phantom study.

5.2.4 - Tumour Tracking of *in-vivo* 0.2 T/0.5 T Equivalent Images

One major disadvantage of the performing *in-vivo* studies is the lack of a true independent gold standard for comparison. While contouring by hand can be

used, the sheer number of images acquired (> 600) makes this less practical. Manually contours may also be susceptible to inter-observer and intra-observer variations. However, from our phantom study it has been shown that the tumour tracking algorithm performs well in high CNR scenarios. Therefore in this study, we applied the auto-contouring algorithm to the original 3 T image with high CNR to obtain reference tumour shape and location. The set of contours generated from the images with CNR reduced to 0.2 and 0.5 T equivalents are compared against set of contours generated with the original 3 T images.

5.2.5 - Tumour Tracking Data Analysis.

After the tumour tracking algorithm is performed on the 3 T patient data, the range of motion of the tumour's centroid in the SI and the AP direction is reported. Centroid measurements of the 0.5 T and 0.2 T equivalent data are then compared to the gold-standard 3 T values. Dice coefficient, between the tumour shapes determined from the original 3 T images and the degraded 0.2 T/0.5 T equivalent images, is calculated to compare the overall contour shape error along with the errors in determining the tumour's centroid.

5.3 - Results and Discussion

5.3.1 - CNR Measurements

The CNR (mean \pm standard deviation) of the patient's tumour in the original 3 T over the 15 sample images is 51.9 ± 5.1 . By applying the linear CNR scaling factor of 6 and 15, the CNR is reduced to 8.7 ± 0.9 for 0.5 T images and 3.5 ± 0.3 for 0.2 T images. Using a 2 sample t-test, these values are determined to be

significantly lower compared to 11.5 ± 1.2 ($p < 0.00001$) and 4.3 ± 0.4 ($p < 0.00001$) measured from the 0.5 T and 0.2 T equivalent phantoms. For the tumour tracking study, the noise is added to reflect the CNR reflected by the lung contrast phantom. The image for 3 T, and the noise added 0.2 T and 0.5 T equivalent images are shown in Figure 5.1.

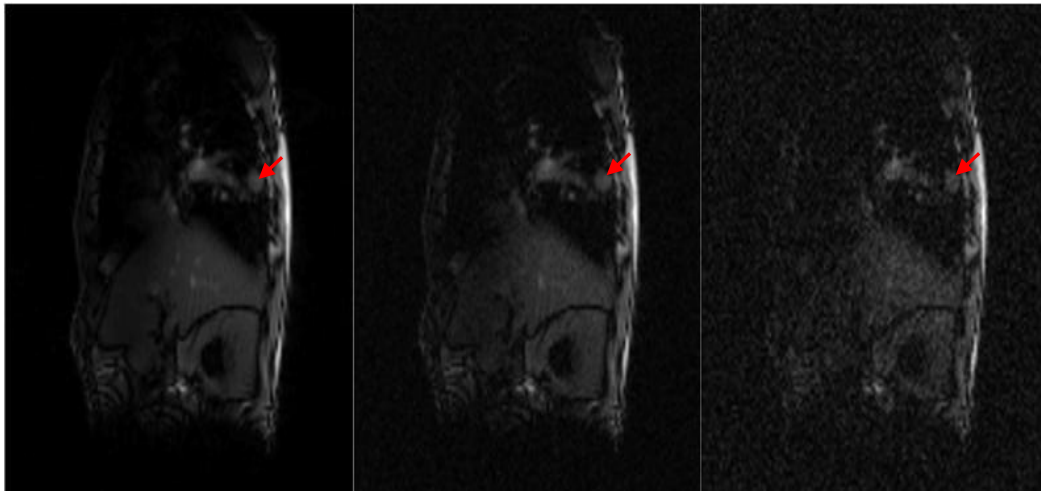


Figure 5-2: Sample dynamic images of the patient for the original 3 T image (left), noise added to reflect 0.5 T CNR (centre) and 0.2 T CNR (right). Lung tumour in each image is indicated by a red arrow.

5.3.2 - Tumour Tracking with 3 T CNR (Gold Standard)

The moving tumour as detected in 3 T dynamic images is tracked successfully segmented in all images by the contouring algorithm. The AP and SI motion patterns of the tumour are shown in Figures 5-3, 5-4, respectively. The maximum extent of motion in the AP and SI direction is 5.7 mm and 26.1 mm, respectively which is the expected pattern of tumour motion in lower lobe.

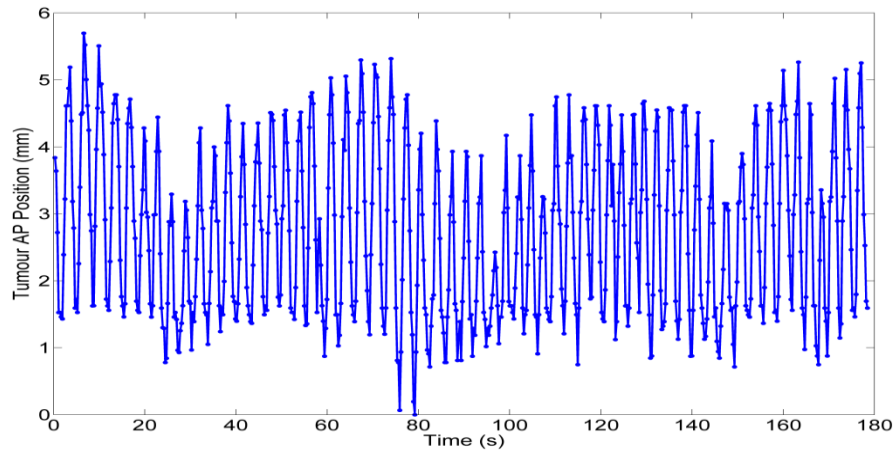


Figure 5-3: Centroid position of auto-segmented tumour (AP) in 3 T images as determined by the auto-contouring algorithm. The maximum range of AP motion is 5.7 mm.

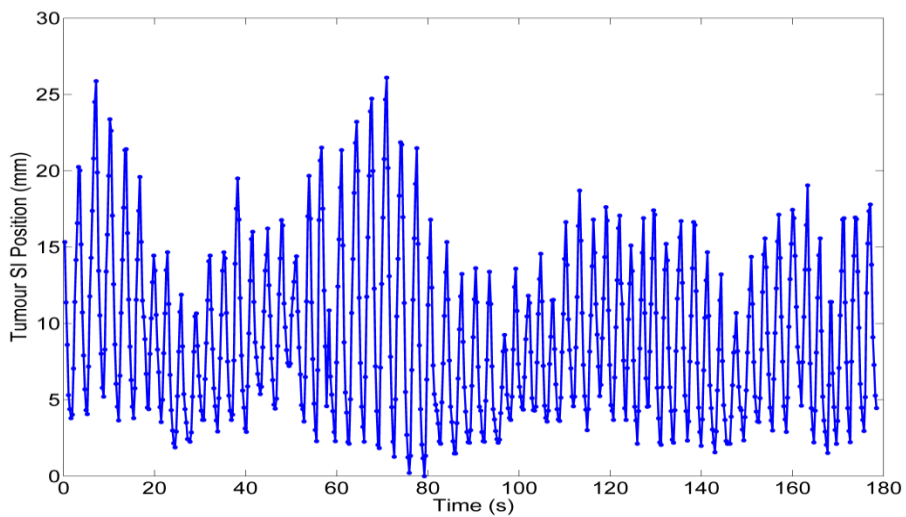


Figure 5-4: Centroid position of auto-segmented tumour (SI) in 3 T images as determined by the auto-contouring algorithm. The maximum extent of SI motion is 26.1 mm.

5.3.3 - Tumour Tracking with 0.2/0.5 T

The 0.2 T and 0.5 T equivalent in-vivo images are tracked using the algorithm and the resulting contours and centroids are compared to the 3 T images. In terms of centroid position, compared to 3 T images, the centroid's RMS error for the 0.5 T dataset is 0.44 mm, and the centroid's RMS error for the 0.2 T equivalent images

is 0.82 mm. These numbers are comparable to those achieved using the phantom images. In terms of mean overall contour shape, the contours from the 0.5 T equivalent images have a mean dice coefficient of 0.95 ± 0.02 compared to the contours at 3 T, and the contours from the 0.2 T equivalent images have a mean dice coefficient of 0.93 ± 0.03 .

5.4 - Discussion

Because the phantom has significantly lower T_1 compared to the patient in original 3 T images, one may expect the 0.2/0.5 T CNR obtained from the phantoms to be higher compared to linearly scaled CNR of the patient images. However, it is also possible that the phantom may not fully replicate the geometry and tissue characteristics of a patient. It would not be possible to verify these CNR values without performing the experiment with a patient in those fields. By performing a two sample t-test, the CNR predicted from the phantom images are determined to be significantly higher ($p < 0.00001$), 23% and 32% for 0.2 T and 0.5 T respectively, compared to the values obtained from linearly scaled patient images. These smaller differences are of the second order in comparison to changing field strengths B_0 i.e. scaling from 3 T to 0.5 T represents a difference of ~600%.

For the purpose of testing the tumour tracking algorithm, we have assumed the CNR values obtained from the phantom experiments to scale down the 3 T patient images. Using those CNR values, we find that the tumour tracking algorithm's accuracy in this *in-vivo* scenario is similar to the results from the phantom study. Centroid RMSE for phantom tumour tracking is < 0.55 mm and < 0.93 for 0.2 T

and 0.5 T equivalents, compared to 0.44 mm and 0.82 mm for the patient. Mean dice coefficients of > 0.96 and > 0.93 are achieved for phantom images, compared to 0.95 and 0.93 for the patient images. This work shows that the tumour tracking accuracy for images is primarily dependent on CNR. Other factors such as tumour shape, motion pattern, or whether the image is acquired *in vitro* and *in vivo* does not have a great impact on tracking accuracy.

Through-plane motion could be problematic for a 2D, beam's eye view image based tumour tracking system, if the tumour moves out of the imaging plane. For this patient, the lung tumour does not appear to move completely out of the imaging plane in any of the images. However, small amounts of through plane motion may still have some impact on the imaged tumour shape, and this impact is not evaluated in this experiment. Through plane motion in the sagittal plane is expected to be limited due to the fact that LR motion is known to be the smaller compared to SI and AP motions [1]. We measured the maximum extent of AP motion to be 7 mm. This would represent the out-of-plane motion for a chosen coronal plane in the dynamic imaging study. The chosen slice thickness of 20 mm in this instance is likely going to be sufficient to ensure the tumour never completely leaves the imaging plane. However, as the extent of out-of-plane motion is likely going to be dependent on the individual patients and the location of the tumour within the lung, a different slice thickness may be required in different clinical scenarios.

Along with the phantom results, these preliminary patient data demonstrate the feasibility of performing the real time tumour tracking at low field. More patient

data, with tumour at different locations within the lung will be acquired in the future. The tracking algorithm should also be evaluated on a series of different imaging planes, as it is unlikely that the coronal and sagittal views will always represent the beam's eye view imaging plane. Eventually, patients should be imaged in a real low field Linac-MR when it becomes available to verify our lung tumour CNR.

5.4 - References

1. Keall, PJ, Mageras GS, Balter JM et al., The management of respiratory motion in radiation oncology report of AAPM Task Group 76. *Medical Physics*, 33(10):3874, 2006.

Chapter 6 - Conclusions

Real time tracking of lung tumours is one of the most promising applications of the proposed Linac-MR system. For such a treatment scheme to work, the low field (0.2 T ~ 0.5 T) MR imaging system must have the ability to generate images at high speeds (~4 fps) while maintaining sufficient image quality for fast, automatic tumour delineation. In this work, we evaluated the feasibility of performing tumour tracking at different low field strengths (0.2 T/0.5 T) using a clinical 3 T MR scanner available.

A linear relationship is often used to approximate changes in image quality (SNR/CNR) with respect to changes in the main magnetic field strength. Some of the MR contrast parameters of tissues (such as T_1) are also dependent on B_0 , and are not accounted for in such a linear relationship. To address this problem, a series of different MR tissue equivalents were built to replicate low field equivalent MR contrast parameters. Appropriate amount of contrast agents are added into the phantom material such that, when placed in a 3 T imager, the equivalent material will have contrast parameters that resemble those of real tissue at lower field strengths. The phantom contains three types of tissues, those of lung tumour (target), surrounding parenchyma (background), and the generic tissues simulators that mimic the noise resistance generated by the patient's body. Balanced SSFP sequence was deemed to be the preferred sequence for real time tumour tracking. A bSSFP sequence can be configured to image at ~ 4 fps while

maintaining an acceptable image resolution. BSSFP was found to generate a greater SNR and CNR when compared to a similar sequence such as FLASH. Dynamic images were acquired with the 0.2 T and 0.5 T equivalent phantoms in the scanner. Noise was added to lower the CNR to the appropriate levels. Using our 0.2 T and 0.5 T equivalent phantoms, the predicted CNR of lung tumours of a 4 fps bSSFP sequence is 4.3 ± 0.4 and 11.5 ± 1.2 , respectively.

The lung contrast phantom was used to evaluate an in-house auto segmentation algorithm. The lung phantom was driven by a motor with pre-programmed 1-D motion that replicates the respiration pattern of the human lung. An external measurement of tumour position was performed by attaching an optical encoding device to the phantom. The performance of the algorithm was evaluated in two ways, by comparing the centroid of the contours to the optical encoder reading, and by comparing the contour shapes to a set of "gold standard" contours. In terms of centroid accuracy, a mean RMSE of < 0.55 mm is achieved for 0.5 T equivalent images, whereas a mean RMSE of < 0.92 mm is achieved for 0.2 T equivalent images. In terms of overall contour agreement, a Dice's coefficient of > 0.96 and > 0.93 were achieved for 0.5 T and 0.2 T equivalent images. Overall, the auto-contouring algorithm was successful in achieving a high degree of accuracy in low field CNR's in phantoms scenarios.

Patient data is expected to present additional problems in tumour tracking, including potential through plane motion of the tumour, as well as the presence of other high contrast structures. Our preliminary data from a single lung cancer patient has shown that the algorithm performed similarly well as compared to the

phantom if the CNR is similar. CNR is also measured from the patient and scaled to 0.2 T and 0.5 T by applying a linear scaling factor. In this particular patient, the measured CNR of tumour region is 23% and 32% lower as compared to those of the tumour region in the lung phantoms.

Our work thus far has shown that MR tumour tracking using low field MRI is indeed feasible. CNR of bSSFP images that can be expected from 0.2 T and 0.5 T scanner at 4 fps is sufficient for the tumour to be segmented automatically in all of our phantom scenarios, and generates similar result with our patient data. For future work, the algorithm should be tested using more patient data in different clinical scenarios. Patients should be scanned with a low field Linac-MR unit when it becomes available. Other possible future work includes the incorporation of MR navigator pulses [1] to guide in 2D slice selection, thus eliminating the problem of through plane motion, which may be a problem in some patients, and developing methods to speed up data acquisition. Unfortunately, most common speed up techniques trades acquisition speed for CNR. While, this may be feasible at 0.5 T, the tracking accuracy will be reduced as a result. Compressed Sensing (CS) techniques may be a potential solution to speed up acquisition with little cost to CNR [2]. Unfortunately, current image reconstruction times will need to be reduced by an order of magnitude for such a method to be useful in real time. This may be possible in the future with Graphical Processor Unit (GPU) implementation of compressed sensing [3].

6.1 References

1. Taylor AM, Jhooti P, Wiesmann F et al., MR navigator echo monitoring of temporal changes in diaphragm position: Implications for MR coronary angiography. *Journal of Magnetic Resonance Imaging* 7(4):629:636, 1997.
2. Lustig M, Donoho D, Pauly JM., Sparse MRI: The Application of compressed sensing for rapid MR imaging. *Magnetic Resonance in Medicine* 58(6):1182-1195, 2008.
3. Kim D, Trzasko J, Smelyanski M et al., High-Performance 3D Compressive Sensing MRI Reconstruction Using Many-Core Architectures. *International Journal of Biomedical Imaging* 2011:473128, 2011

Bibliography

- Bergin CJ, Glover GH, and Pauly JM., Lung Parenchyma - Magnetic-Susceptibility in MR Imaging. *Radiology* 180:845, 1991.
87
- Bernstein MA, King KF, Zhou XJ, Handbook of MRI pulse sequences. Academic Press, 2004.
44, 45, 47, 55, 87
- Boss A, Schaefer S, Martirosian P et al., Magnetic resonance imaging of lung tissue: Influence of body positioning, breathing and oxygen inhalation on signal decay using multi-echo gradient-echo sequences. *Investigative Radiology* 43:433, 2008.
59
- Bottemley PA, Hardy CJ, Argersinger RE and Allenmoore G., A Review of H-1 Nuclear-Magnetic-Resonance Relaxation in Pathology - Are T1 and T2 Diagnostic? *Med. Phys.* 14:1, 1987.
54, 58, 59, 68
- Cheng CW, Wong J, Grimm L., Commissioning and Clinical Implementation of a sliding gantry CT scanner installed in an existing treatment room and early clinical experience for precise tumour localization. *American Journal of Clinical Oncology*. 26(3):e23, 2003.
7
- Dawson, LA., Jaffray, LA., Advances in Image Guided Radiation Therapy. *Journal of Clinical Oncology* 25(8):938, 2007.
5
- Fallone, BG, Murray B, Rathee S et al., First MR images obtained during megavoltage photon irradiation from a prototype integrated linac-MR system. *Medical Physics*, 36(6):2094, 2009.
14
- Flear CTG, Carpenter RG, and Florence I, Variability in the water, sodium, potassium, and chloride content of human skeletal muscle. *Journal of Clinical Pathology* 18:74, 1965.
62

Gudbjartsson H and Patz S, The Rician Distribution of Noisy MRI Data. Magnetic Resonance in Medicine, 34(6):910, 1995.	49
Haddad FS, Somsin AA, Seeding and perineal implantation of prostate cancer in the track of the biopsy needle: three case reports and a review of literature. Journal of Surgical Oncology, 35:184, 1987.	6
Hanley J, Debois MM, Mah D et al., Deep inspiration breath-hold technique for lung tumours: The potential value of target immobilization and reduced lung density in dose escalation. International Journal of Radiation Oncology Biology Physics. 45(3), 603, 1999.	11
Hatabu H, Alsop AC, Listerud J et al., T2* and proton density measurement of normal human lung parenchyma using submillisecond echo time gradient echo magnetic resonance imaging. European Journal of Radiology 29:245, 1999.	57
Health Canada, Economic Burden of Chronic Illnesses in Canada 1998, 2002.	1
International Commission of Radiation Units and Measurements (ICRU), ICRU Report 50 "Prescribing, Recording, Reporting Photon Beam Therapy, 1993.	3
Jaffray, DA, Siewerdsen, JH, Wing JW, Martinez, AA, Flat-panel cone-beam computed tomography for image-guided radiation therapy. International Journal of Radiation Oncology Biology Physics. 53:1337, 2002.	7
Kato H, Kuroda M, Yoshimura et al., Composition of MRI phantom equivalent to human tissues. Med. Phys. 32:3199, 2005.	60
Keall, PJ, Mageras GS, Balter JM et al., The management of respiratory motion in radiation oncology report of AAPM Task Group 76. Medical Physics, 33(10):3874, 2006.	9, 10, 11, 12, 13, 86, 96

Kim D, Trzasko J, Smelyanski M et al., High-Performance 3D Compressive Sensing MRI Reconstruction Using Many-Core Architectures, International Journal of Biomedical Imaging 2011:473128, 2011.	100
Kirkby C, Murray B, Rathee S, Fallone BG, Lung Dosimetry in a linac-MRI radiotherapy unit with a longitudinal magnetic field. Medical Physics, 37(9):4722, 2010.	15
Lagerwaard FJ, Van Sornsens de Koste, JR, Nijssen-Vosser, MR et al., Multiple "slow" CT scans for incorporating lung tumour mobility in radiotherapy planning. International Journal of Radiation Oncology Biology Physics, 51(4):932, 2001.	9
Langen KM., Jones DT, Organ Motion and Its Management. International Journal of Radiation Oncology, Biology and Physics, 50:265, 2001.	6
Laughlin, JS, Development of Technology of Radiation Therapy. Radiography, 9(6):1245, 1989.	2
Levitt MH, Spin Dynamics: Basics of Nuclear Magnetic Resonance John Wiley and Sons, West Sussex, England, 2008.	53
Lustig M, Donoho D, Pauly JM, Sparse MRI: The Application of compressed sensing for rapid MR imaging. Magnetic Resonance in Medicine 58(6):1182-1195, 2008.	100
Mackie, TR, Kapatoes, J, Rachala, K, et al., Image guidance for precise conformal radiotherapy. International Journal of Radiation Oncology Biology and Physics 56(1):89, 2003.	13
Murphy MJ, Adler JR, Modduluri M. et al., Image guided radiosurgery for the spine and pancreas, Comput. Aided Surgery 5(4):278, 2000.	14

Nishimura DG, Principles of Magnetic Resonance Imaging, 1996.	21, 25, 26, 48, 50, 51
Oborn, BM, Metcalfe PE, Rosenfeld AB, Butson MJ, Monte Carlo Characterization of skin doses in 6 MV transverse MRI-linac systems: Effect of field size, surface orientation strength, and exit bolus. Med. Phys, 37(10):5208, 2010.	16
Och JG, Clarke GD, Sobol WT et al., Acceptance Testing of Magnetic- Resonance-Imaging Systems - Report of Aapm Nuclear-Magnetic-Resonance Task Group No-6. Med. Phys. 19:217, 1992.	61
Plathow C, Klopp M, Fink C et al., Quantitative analysis of lung and tumour mobility: comparison of two time-resolved MRI sequence. The British Journal of Radiology 78:836, 2005.	15
Raaymakers BW, Lagendijk JJW, Overweg J et al., Integrating a 1.5T MRI scanner with a 6 MV accelerator: proof of concept. Phys Med Bio. 54:N229, 2009.	8
Redpath PW, Signal-to-noise ratio in MRI. British Journal of Radiology 71:704, 1998.	52
Rodgers MS, Collinson R, Desai et al., Risk of dissemination with biopsy of colorectal liver metastases. Dis Colon Rectum 46:454, 2003.	6
Scheffler K and Hennig J, Is TrueFUSP a gradient-echo or a spin-echo sequence? Magnetic Resonance in Medicine 49:395, 2003.	47
Scheffler K and Lehnhardt S, Principles and applications of balanced SSFP techniques. European Radiology 13: 2409, 2003.	87

Schmidt HC, Tscholakoff D, Hricak D, and Higgins CB, MR Image-Contrast and Relaxation-Times of Solid Tumours in the Chest, Abdomen, and Pelvis. *Journal of Computer Assisted Tomography* 9:738, 1985.

57, 62

Suh Y, Dieterich S, Cho B, and Keall PJ, An analysis of thoracic and abdominal tumour motion for stereotactic body radiotherapy patients. *Phys. Med. Biol.* 53, 3623, 2008.

74

Taylor AM, Jhooti P, Wiesmann F et al., MR navigator echo monitoring of temporal changes in diaphragm position: Implications for MR coronary angiography. *Journal of Magnetic Resonance Imaging* 7(4):629-636, 1997.

100

Underberg RW, Lagerwaard FJ, Slotman BJ et al., Use of maximum intensity projections (MIP) for target volume generation in 4DCT scans for lung cancer, *International Journal of Radiation Oncology Biology Physics*, 63(1):253, 2005.

10

Van Dyk, J., *The Modern Technology of Radiation Oncology*. (Madison: Medical Physics Publishing), 1999.

1, 2, 3

Verellen, D, De Ridder, M, Linthout et al., Innovations in image-guided radiotherapy, *Nature* 7:949, 2007.

6, 7

Walter C, Heggemann, JB, Wertz, H et al., Phantom and in vivo measurements of dose exposure by image-guided radiotherapy (IGRT): MV portal images vs. kV portal images vs. cone-beam CT. *Radiotherapy and Oncology* 85:418, 2007.

8

Wieben O, Francois C, and Reeder SB, Cardiac MRI of ischemic heart disease at 3 T: Potential and challenges. *European Journal of Radiology* 65:15, 2008.

87

World Health Organization. *World Health Statistics 2008*, 2008.

1

Xiang QS, *University of British Columbia Physics 542 Notes*, 2007.

23, 28, 29, 30, 31, 32, 38, 43

Yun J, Mackenzie M, Robinson D et al., Real-Time MR Tumour Tracking Using a Linac-MR system. *Med. Phys.*, 37: 3153, 2010.

77